Calcium dynamics tune developmental tempo to generate evolutionarily divergent axon tract lengths

Feline W. Lindhout[1], Hanna M. Szafranska[1], Ivan Imaz-Rosshandler[1], Luca Guglielmi[1], Maryam Moarefian[2,4], Kateryna Voitiuk[2,3,4], Natalia K. Zernicka-Glover[1], Daniel J. Lloyd-Davies Sánchez[1], John Minnick[2,4], Mircea Teodorescu[2,3,4], Madeline A. Lancaster[1,5]

[1] MRC Laboratory of Molecular Biology, Cambridge Biomedical Campus, Francis Crick Avenue, Cambridge, UK
[2] Department of Electrical and Computer Engineering, University of California, Santa Cruz, Santa Cruz, CA, USA
[3] Department of Biomolecular Engineering, University of California, Santa Cruz, Santa Cruz, CA, USA
[4] UC Santa Cruz Genomics Institute, University of California, Santa Cruz, Santa Cruz, CA, USA
[5]Cambridge Stem Cell Institute, University of Cambridge, Cambridge, UK

ABSTRACT

The considerably slow pace of human brain development correlates with an evolutionary increase in brain size, cell numbers, and expansion of neuronal structures, with axon tracts undergoing an even greater evolutionary increase than other neuronal domains. However, whether tempo is responsible for these differences in magnitude, and how, remains to be determined. Here, we used brain organoids to investigate this and observed that human axon tracts spend more time growing and extend farther compared to those of mice, independent of their tissue environment. Single cell RNA sequencing analysis pointed to a subset of calcium-permeable ion channels expressed throughout neuron development, including during axon tract outgrowth. Calcium imaging during early neuron development consistently revealed a reduced calcium influx in human neurons compared to mouse neurons. Stimulating calcium influx and increasing cAMP levels resulted in premature halting of axon tract outgrowth and shorter axon tracts, mimicking the mouse phenotype, while abrogating calcium influx led to an even longer phase of axon tract outgrowth and longer axon tracts in humans. Thus, evolutionary differences in calcium regulation set the tempo of neuronal development, by extending the time window to foster the more elaborated human neuron morphology.

Keywords: developmental tempo, brain development, neuronal maturation, human evolution, axon, neuron morphology

INTRODUCTION

The most striking features that characterize the human brain relate to differences in magnitude. The human brain is larger than that of other primates and rodents, is composed of increased cell numbers, and displays increased neuron size and connectivity[1–3]. These differences in magnitude correlate with differences in the tempo of brain development, with the later stages of cortical neuron morphogenesis being especially protracted in humans, extending up to 5 or even 25 years depending on the brain region[4–9]. During this developmental time window, neurons establish the distinct structures that underpin neuronal connectivity, including axons, dendrites and synapses. Each of these neuronal domains has expanded by several orders of magnitude in humans, with axon tracts and white matter showing an even greater increase compared to synapse numbers and dendritic arbors[7,10–14]. This disproportionate increase of axon tracts is due to axons needing to extend farther in a larger brain and, similar to dendrites, the need to expand to accommodate the increase in synapse number per neuron. Thus, a consistent correlation between developmental tempo and evolutionary expansion is observed across species, with the tempo of neuronal morphogenesis being particularly divergent in humans. This has led to the hypothesis that the more elaborate structure of the human brain is due to a slowing of tempo, or bradychrony[15,16]. However, a direct link between tempo and morphological complexity is still lacking.

The developmental tempo of the human brain compared with that of mice seems to follow a different and even more protracted evolutionary pattern compared with the rest of the body, which is only ~2-fold slower in humans than mice[17–20], pointing to distinct underlying mechanisms. With the advancements of human neural *in vitro* models, mechanisms driving the tempo of neurodevelopment are starting to be explored. This has revealed that timing is cell-intrinsic, as species-specific developmental tempo is maintained when transplanting human neurons into rodent brains, or in neuron co-cultures from different species[21–23]. Recent studies have pointed to a role for mitochondria metabolism[24] and epigenetics[25], as perturbing these processes can accelerate the timing of acquisition of features of mature neurons, including dendritic arborization, synapse number, and electrophysiological activity. However, altering tempo in this manner did not result in differences in phenotype that align with the evolutionary pattern, namely decreased neuronal complexity with faster development. Thus, a mechanistic explanation for both the evolutionarily slowed tempo of human neuron morphogenesis and its increased morphological complexity has not yet been described.

Investigating a causal relationship between the elaboration of neuron structures and the duration of the process during which it is established is challenging in human models. Precisely because of the extended time of human brain development it is difficult to capture the end point when neuronal development is complete and structural complexity can be

assessed. Axon tract development is a process of neuron morphogenesis completed during embryogenesis, making it a more accessible process to study, and the expansion of axon tracts are also a perfect example of the evolutionary elaboration of neuronal structures. However, whilst other maturation hallmarks are easier to read out using typical models such as 2D cultures, it is considerably more challenging to analyse axon length using such cultures. Here, we used modified human and mouse brain organoid slice cultures that are capable of forming self-organised axon tracts, and combined these with tailored micropatterned devices to mechanistically explore the link between developmental tempo and evolutionary axon tract morphology. Using these methods, we found that human organoids consistently exhibited a lower calcium influx, which was largely mediated by L-Type voltage-gated calcium channels (VGCC), than mice at stage-matched timepoints. Increasing the L-Type VGCC-mediated calcium influx or cAMP levels in human neurons mimicked the mouse phenotype, leading to a shortening of the axonogenesis time window as well as shortened axon tracts. The opposite effect was observed upon blocking L-Type VGCC-mediated calcium influx, resulting in axon tracts that grew for a longer time and extended beyond their normal length. Thus, this work has uncovered a calcium-mediated mechanism that drives species-specific developmental tempo by tuning the duration of a development stage, thereby demonstrating a causal relationship between tempo and evolutionary neuronal morphology.

RESULTS

Human organoid axon tracts take longer to establish and grow longer than mouse

Tempo could refer to various potential biological rates. To enable a more elaborate final product, we hypothesised that the relevant difference in tempo would be one that affects the duration of transient developmental states during which neuronal structures form (Fig 1a). For the purposes of axon tract length, the relevant state would be axon tract outgrowth. Therefore, to investigate evolutionary differences in axon tract outgrowth and the eventual morphology of axon tracts, we used human and mouse brain organoid slice cultures generated using an unguided method, as these most closely resemble *in vivo*-like tempo (Supplementary Fig 1a), while guided protocols often unfold at a several times faster pace[26]. In order to generate comparable organoids of the proper cerebral cortical identity, human and mouse brain organoids were generated using an identical method, with the timing of media changes during pluripotency exit and neural induction tailored to match the species-specific differentiation, as described before[27]. Over the course of their development, the organoids exhibited a gradual size divergence, culminating in a substantial enlargement in human organoids, reminiscent of *in vivo* differences in human and mouse brain sizes (Fig 1b).

Figure1

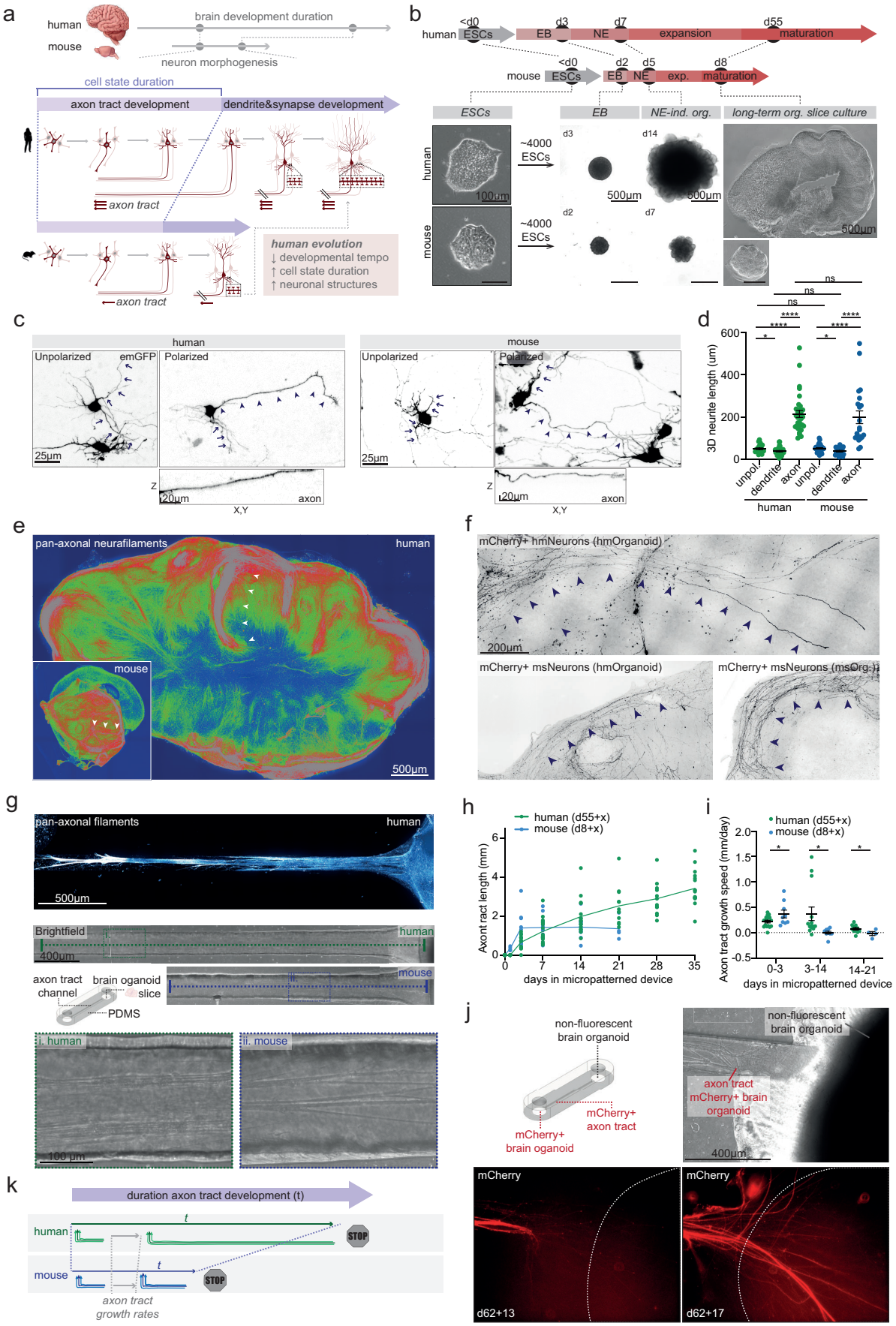
a
human
mouse
brain development duration
neuron morphogenesis
cell state duration
axon tract development
dendrite&synapse development
axon tract
human evolution
↓ developmental tempo
↑ cell state duration
↑ neuronal structures
axon tract
b
human
<d0
ESCs
d3
EB
d7
NE
expansion
d55
maturation
mouse
<d0
ESCs
d2
EB
d5
NE
exp.
d8
maturation
ESCs
EB
NE-ind. org.
long-term org. slice culture
human
mouse
~4000 ESCs
~4000 ESCs
d3
d14
d2
d7
100µm
500µm
500µm
500µm
c
human
Unpolarized
emGFP
Polarized
25µm
20µm
axon
X,Y
mouse
Unpolarized
Polarized
25µm
20µm
axon
X,Y
d
3D neurite length (um)
unpol.
dendrite
axon
human
mouse
e
pan-axonal neurafilaments
human
mouse
500µm
f
mCherry+ hmNeurons (hmOrganoid)
200µm
mCherry+ msNeurons (hmOrganoid)
mCherry+ msNeurons (msOrganoid)
g
pan-axonal filaments
human
500µm
Brightfield
human
400µm
axon tract channel
brain oganoid slice
PDMS
mouse
i. human
ii. mouse
100 µm
h
human (d55+x)
mouse (d8+x)
Axont ract length (mm)
days in micropatterned device
i
human (d55+x)
mouse (d8+x)
Axon tract growth speed (mm/day)
0-3
3-14
14-21
days in micropatterned device
j
non-fluorescent brain organoid
mCherry+ axon tract
mCherry+ brain oganoid
non-fluorescent brain organoid
axon tract mCherry+ brain organoid
400µm
mCherry
d62+13
mCherry
d62+17
k
duration axon tract development (t)
human
t
STOP
mouse
t
STOP
axon tract growth rates

Figure 1: Duration of axon tract development is longer with axon tracts extending farther in human brain organoids independent of environmental context a. Schematic illustration of a hypothesised model where developmental tempo may explain neuronal complexity. b. Protocol timeline for the generation of unpatterned human and mouse ALI-COs using the same protocol steps for both species, with the timing of each step tailored to the species-specific timing [27]. Brightfield images reflect representative images at different steps of the protocol. c. Representative images of sparsely labelled emGFP-positive unpolarized and polarized neurons in human and mouse ALI-COs. Zoom shows a line plot of the axons in Z. d. Quantifications of 3D neurite length in sparsely labelled emGFP-positive neurons in human (day 57-59) and mouse (day 10-11) ALI-COs, including the 3D length of unpolarised neurites (marked by arrows) in unpolarised neurons, and the 3D length of the longest dendrite (marked by arrows) and the axon (marked by arrowheads) in polarised neurons. Hm unpolarized: n=22 neurons, Hm dendrite: n=32, Hm axon 8: n=32, Ms unpolarized: n=78 neurons, Ms dendrite: n=48, Ms axon 8: n=48. e. Long-range axonal tracts with similar morphologies in a day 69 human and a day 15 mouse ALI-CO immunostained for pan-axonal neurofilaments, with axon tracts extending further in humans (indicated by arrowheads). f. Axon bundles (indicated by arrowheads) of dissociated human and mouse neurons transplanted on human or mouse ALI-COs. g. Top: human organoid slice culture placed in a micropatterned device at day 55, fixed 35 later, and immunostained for pan-axonal filaments. Middle: schematic illustration of micropatterned PDMS devices with long channels enabling analysis of outgrowing axon tracts from brain organoid slices. Brightfield images of human (day 55+35) and mouse (day 8+8) organoid slice cultures with an axon tract extending into the channel of the micropatterned device. Bottom: zoom shows self-organised axon tract bundling in both species. h. Quantifications of outgrowing axon tract length of human and mouse brain organoid slice cultures in micropatterned devices over time. Hm day 1: n=21 organoids, Hm day 3: n=17, Hm day 7: n=20, Hm day 14: n=16, Hm day 21: n=12, Hm day 28: n=12, Hm day 35: n=17, Ms day 1: n=4, Ms day 3: n=9, Ms day 7: n=11, Ms day 14: n=11, Ms day 21: n=4. i. Quantifications of axon tract outgrowth rates of human and mouse brain organoid slice cultures in micropatterned devices over time. Hm day 0-3: n=17 organoids, Hm day 3-14: n=14, Hm day 14-21: n=11, Ms day 0-3: n=9 organoids, Ms day 3-14: n=9, Ms day 14-21: n=4. j. Schematic illustration of experimental set-up for the target tissue experiment. RFP-positive axons from an RFP-positive human brain organoid slice culture in a short micropatterned device channel extending on to another non-fluorescent human organoid, outline indicated by dashed line, 12 days and 18 days after being placed in the chamber (at day 62). k. Schematic illustration summarising findings, showing initially a subtly slower axon growth in human, then longer duration of axon tract outgrowth phase.Hm, human. Ms, mouse. All data are shown as mean ± SEM; $^{*}P < 0.05$, $^{****}P < 0.0001$ as determined by unpaired *t* tests.

To study axon tract development, which occurs at relatively later stages of neurodevelopment, we generated long-term air-liquid interface cerebral organoid (ALI-CO) cultures, which we have previously shown to successfully recapitulate various stages of neuronal development with improved neuronal survival[27,28]. For cross-species analysis of axon tract development, we sought to identify a stage-matched timepoint corresponding to the onset of axon development, which was then selected as the day for organoid slicing in each species. Axon development begins when neurons undergo a symmetry break, transitioning from an unpolarized to a polarized state, which involves the accelerated outgrowth of a single neurite that will become the axon[29]. We identified this transition using a sparse viral labelling approach enabling assessing individual morphologies of the different neuronal polarity states in organoids (Fig

1c, Supplementary Fig 1b). Similar to *in vivo*, neuron development in these brain organoids is asynchronous. Thus, we aimed to identify the timepoint where mouse and human exhibited similar numbers of polarized and unpolarized neurons. We observed that in human organoids sliced at day 55, about half of the neurons were still unpolarized (Supplementary Fig 1c). The equivalent level was found for mouse sliced at day 8 (Supplementary Fig 1c). Thus, we successfully stage-matched mouse and human organoids to allow accurate comparison of developmental tempo and morphological outcome.

At the start of neuron development, human and mouse neurons initially displayed similar morphologies, including comparable neurite lengths and soma areas (Fig 1d, Supplementary Figs 1d-h). In both human and mouse neurons, axon lengths were increased compared to other neurite lengths, with dendrites retaining similar lengths as unpolarised neurites, consistent with the notion that dendrite development occurs at later stages (Fig 1d). Moreover, similar to previous reports, human and mouse neurons showed a subtle trend toward a decreased soma area upon establishing neuronal polarity or in timepoints corresponding with the onset of neuronal polarity (Supplementary Figs 1d,e)[30].

Once neuronal polarity was established, and the ALI-COs were allowed to reach a more mature stage, both human and mouse organoids developed self-organised long-range axon tracts projecting to local and distant regions within the ALI-CO, as described previously (Fig 1e)[27,28]. Notably, at these late stages, human axon tracts extended farther than those of mice, mirroring the *in vivo* differences in axon tract length.

Species-specific differences in axon tract length correlate with timing and are cell-intrinsic

In the brain, distinct axon trajectories are established through interactions with the tissue environment, such as stiffness, chemoattractants, and chemorepellents, that influence growth cone turning events and outgrowth rates[31,32]. Across species with different brain sizes, homologous axon trajectories can be identified and follow similar paths with the main difference being their length. Such a difference could be due to differences in developmental tempo of the axon growth stage as well as species-specific factors in the tissue environment. To test these possibilities, we transplanted dissociated mouse neurons onto human and mouse ALI-COs, and observed that they still exhibited similar axon lengths, whereas dissociated human neurons on human ALI-COs developed longer axon trajectories, suggesting that evolutionary differences in axon tract length are intrinsic (Fig 1f).

The fact that human organoids grew longer axon tracts over a more extended time period suggested that the difference in length may relate directly to developmental tempo. To assess this, and to enable detailed investigations of axon tract outgrowth, we sought to establish a method to examine isolated outgrowing axon tracts from each species in a similar and controlled environment. We engineered micropatterned devices from molds generated using photolithography, with chambers for brain organoid slices connected to a 5 mm long channel, to capture outgrowing axon tracts and allow for their unrestricted growth (Fig 1g, Supplementary Figs 2a-c). Within a few days after placing a human brain organoid in one of the chambers, individual axons started to grow out into the channel and continued to extend in subsequent weeks whilst forming large self-organised tracts, similar to those observed in ALI-COs (Fig 1g). The tract was almost completely composed of axons with a few neurons migrating into the tract once axons started to bundle, some of these integrating with axons in the tract, similar to the interstitial white matter neurons *in vivo*[33,34], whilst others underwent apoptosis, akin to programmed cell death of misoriented neurons during brain development[35,36] (Supplementary Figs 2d,e).

We observed a similar axon tract outgrowth pattern of mouse brain organoids in micropatterned devices, but with the important difference that axon tracts from mouse organoids did not extend as far compared to human (Fig 1g). Moreover, by examining axon tract development over time, we observed that the longer axon tracts of human organoids were not due to increased axon outgrowth rates (Fig 1h,i). In fact, initial axon outgrowth rates were faster in mice (Figs 1i), similar to the trend that we observed when comparing young polarised neurons in human and mouse ALI-COs (Supplementary Fig 1f). However, the parameter that consistently correlated with species-specific differences in axon tract length was the time window of the axon tract outgrowth stage, with axon tract growth halting after about 3 days in mouse compared to about 5 weeks in human.

These findings indicate that, during the axon tract outgrowth phase, axons follow a cell-intrinsic program where they are committed to extending for a predetermined time window, and during which they are not yet receptive to environmental interactions that may direct synapse formation. This also explains how, in ALI-COs as well as *in vivo*, axons initially pass by neurons of similar identities as of those they eventually target. To further test this, we examined the effect of axon outgrowth when it is presented with a target tissue whilst still in the axon extension stage. Using similar micropatterned devices, but with shorter channels, we placed a human brain organoid slice expressing mCherry in one chamber, and a non-fluorescently labelled human brain organoid in the other chamber (Fig 1j). Indeed, after ~12 days in culture, corresponding with the axon tract outgrowth stage in human organoids (Fig 1j), human axons

had reached the target tissue, but this did not result in axon outgrowth halting. Instead, axons grew over the target tissue and continued to do so in subsequent days (Fig 1j). This was also observed when using mouse spinal cord explant as target tissue, which we have previously shown to be functionally innervated by outgrowing axon tracts from human brain organoid slices[28], with axons from human brain organoids labelled with Marcks-GFP extending over the mouse spinal cord tissue whilst in their axon elongation stage (Supplementary Fig 2f). These findings, together with extensive previous work on axon pathfinding, suggest multiple layers of control in establishing axon tract length: a species-specific time window of the axon elongation stage, which underlies interspecies differences in axon tract length, combined with the well-described interactions with environmental factors that underlie different directionalities and lengths of axon tracts within the brain[31,32]. Moreover, these data indicate that developmental tempo, irrespective of species-specific tissue environment, tissue size and target tissue interactions, consistently correlates with species-specific differences in axon tract length (Fig 1k).

Transcriptome profiling points to calcium-permeable ion channels

To identify a molecular mechanism that could underlie changes in species-specific tempo and axon tract length, we performed single-cell RNA sequencing of 13 human and 8 mouse timepoints, capturing timepoints identified to reflect the dynamic onset of axon formation through to stages beyond axon halting (Fig 2a, Supplementary Figs 3a,b). Both human and mouse brain organoids displayed forebrain identities, exhibiting a wide range of neural cell types and complexity, as expected[28,37,38]. Cluster analysis revealed the presence of clusters representing different stages of cortical neurogenesis in both human and mouse samples, as indicated by the presence of markers of neural progenitors and neurons across different maturation stages (Fig 2a). Additionally, we identified clusters with other forebrain identities, including choroid plexus in human samples, retinal progenitors, retinal photoreceptors, and retinal pigment epithelium cell clusters in mouse samples (Fig 2a). The human dataset also exhibited a small cluster that lacked clear differential gene expression and was generally positive for markers of all cell identities. The cells in this small cluster all originated from only two out of 48 samples, which exhibited a profoundly lower cell count compared to all other samples, suggesting ambient RNA from debris.

We also identified a cluster representing mitotic radial glia, as well as a gliogenesis cluster in the mouse samples, which, as expected, mostly originated from more mature samples (Fig 2a, Supplementary Fig 3b). Specifically, in this cluster, we observed the presence of various glia progenitors, including gliogenic radial glia and oligodendrocyte precursor cells, and glia subtypes, including oligodendrocytes and astrocytes (Fig 2a).

Figure 2

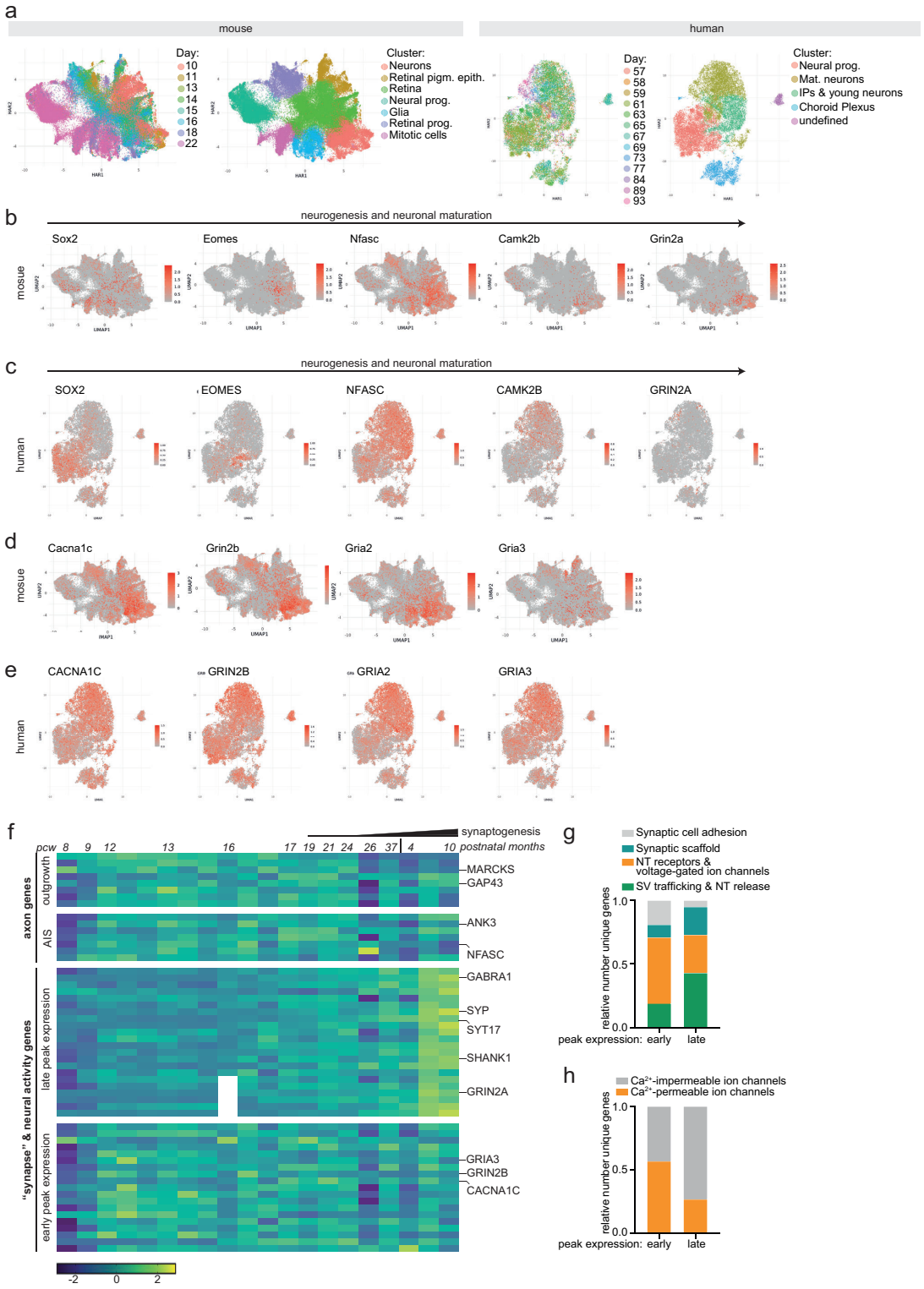

Figure 2: A subset of calcium-permeable ion channels show increased expression during early neuron development in human and mouse a. UMAP of the transcriptomic landscapes from scRNA-seq of human and mouse organoids. Cells are colored by timepoints or clusters. b. UMAP feature plots of mouse scRNA-seq for

Sox2 (neural progenitors), Eomes (intermediate progenitors), Nfasc (axon initial segment), Camk2b (synapses) and Grin2a (mature synapses). c. UMAP feature plots of human scRNA-seq for SOX2 (neural progenitors), EOMES (intermediate progenitors), NFASC (axon initial segment), CAMK2B (synapses) and GRIN2A (mature synapses). d. UMAP feature plots of mouse scRNA-seq for Cacna1c Grin2b, Gria2, Gria3. e. UMAP feature plots of human scRNA-seq for CACNA1C, GRIN2B, GRIA2 and GRIA3. f. Heatmap of RNA expression data (z scores of log2 RPKM values) from the human prefrontal cortex *in vivo* (data from Brainspan), showing temporal expression profiles of genes expressed at embryonic and early postnatal timepoints. g. Relative proportions of genes encoding for "synapse" proteins with early, well before increased appearance of synaptic structures, and late, corresponding with increased appearance of synaptic structures, developmental RNA peak expression across different synaptic subcategories. h. Relative proportions of genes encoding for "synaptic" ion channels with early and late developmental RNA peak expression, categorised on calcium permeability upon activation. pcw, postconception week; AIS, axon initial segment.

In addition to different cell types, we could also distinguish a clear progression of neuronal maturation, with expression of genes encoding for axon outgrowth and axon initial segment proteins during the transition from neural progenitors to neurons, followed by an increase of synaptic genes (Figs 2b,d). In a small subset of the most mature neurons in both the human and mouse datasets, which were exclusively present at the latest timepoints, we could already detect the mature synapse marker Grin2a (Figs 2b,d), indicating a full coverage of the neuronal maturation stages in our datasets. The distinct developmental RNA expression profiles of various neuronal maturation genes were confirmed to correlate with their corresponding protein expression patterns (Supplementary Figs 3c,d).

To identify relevant regulators of stage transitions that may be involved in differences in the tempo and length of axons, we looked for genes that had a dynamic expression profile corresponding with the early and subsequent maturation stages of neuron development. When analysing the developmental expression profiles of these neuronal maturation genes in human and mouse datasets, we observed that a subset of genes related to neural activity and synapses were expressed during early stages, with an expression profile that was similar to axon outgrowth and axon initial segment genes instead of other synaptic and neural activity genes (Figs 2d,e). Similar developmental expression dynamics of these genes were observed when analysing RNA sequencing data from the human prefrontal cortex *in vivo* (Fig 2f). The identity of these genes appeared biased toward synaptic cell adhesion molecules, which are known to play important roles in axon guidance prior to synapse formation, as well as synaptic neurotransmitter receptors and voltage-gated ion channels (Fig 2g). Notably, among the ion channels, they included relatively more ion channels that become permeable to calcium upon activation (Fig 2h). The expression profile of these calcium channels, combined with the well-established role of calcium in many processes of neuronal morphogenesis[25,39–48], led us to

investigate whether calcium dynamics might underlie the evolutionary diversification of neuronal morphologies.

Species-specific differences in calcium dynamics at stage-matched timepoints

To examine calcium dynamics in axon tracts during neuronal development, we used the GCaMP7f reporter to investigate species-specific differences in neural activity modes present across developmental stages. This includes spontaneous calcium transients that gradually transition to synchronous bursts, before the shift to asynchronous networks that starts as synaptic structures begin to increase (Supplementary Fig 4a). In both human and mouse organoids, we observed spontaneous calcium transients during early neuron development stages (Figs 3a,b, Supplementary videos 1,2), with the appearance of synchronous calcium bursts increasing over time (Figs 3c,d, Supplementary videos 3,4). The transition from spontaneous to synchronous activity occurred around day 76 in human organoids and day 17 in mouse organoids (Fig 3e,f), which also corresponded with the onset of gliogenesis in each species (Supplementary Figs 4b-d), providing a carefully stage-matched timepoint for subsequent analyses (Fig 3g). To identify the timepoints reflecting the start of asynchronous networks, we assessed the number of synapses over time, as measured by co-localisation of pre- and postsynaptic puncta (Supplementary Figs 4e,f,i), which gives a more reliable read-out compared to analysing individual puncta (Supplementary Figs 4g,h,j,k). Similar to *in vivo*, a few synapses were already present during early stages, but only began to significantly increase at day 146 in human ALI-COs and day 29 in mouse ALI-COs, thus indeed considerably later than the onset of synchronous burst activities (Supplementary Fig 4a).

We then performed a cross-species analysis of calcium dynamics at matched timepoints during spontaneous activity, corresponding with day 69 in human and day 15 in mouse, and synchronous activity, occurring at day 82 in human and day 19 in mouse. At both stages and neural activity modes, we observed a consistently lower amplitude, but not frequency, in human compared to mouse axons (Figs 3h-j, l-n). Calcium transient durations were also shorter in human during spontaneous activity, with no differences during synchronous burst activity (Figs 3k,o). We also compared proximal, mid and distal regions of axon tracts and observed very similar parameters along the length of axons, suggesting a consistent species-specific difference irrespective of location on the axon tract (Supplementary Fig4l-q). The identified species-specific differences in calcium dynamics thus displays a quantitative difference at matched developmental stages. This suggests that calcium dynamics not only correlate with tempo but represent a strong candidate mechanism for setting tempo.

Figure 3

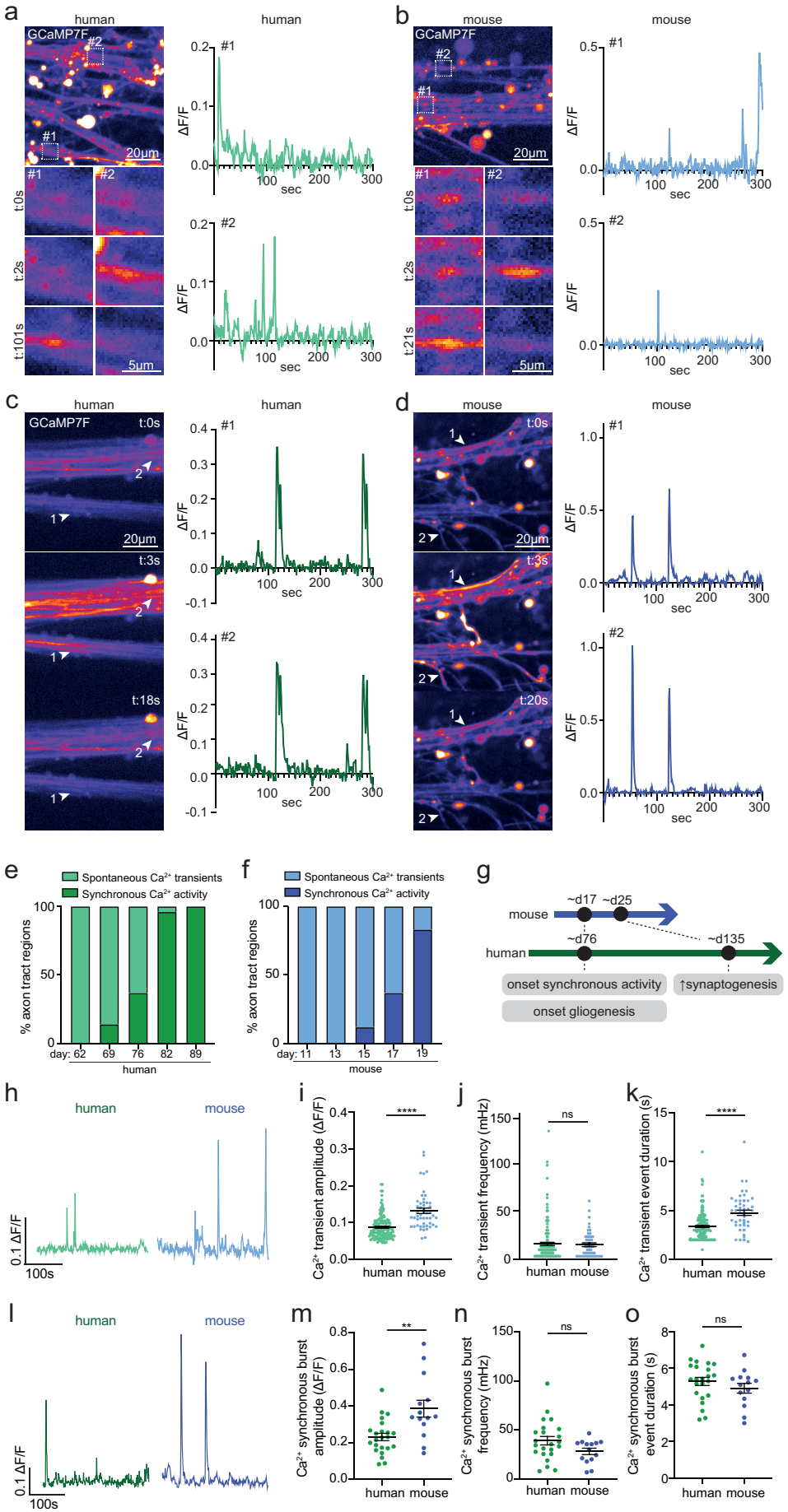
a
human
GCaMP7F
#1
#2
20µm
5µm
t:0s
t:2s
t:101s
ΔF/F
sec
b
mouse
t:21s
c
t:3s
t:18s
d
t:20s
e
Spontaneous Ca2+ transients
Synchronous Ca2+ activity
% axon tract regions
day: 62 69 76 82 89
f
day: 11 13 15 17 19
g
~d17 ~d25
~d76
~d135
onset synchronous activity
↑synaptogenesis
onset gliogenesis
h
0.1 ΔF/F
100s
i
Ca2+ transient amplitude (ΔF/F)
****
j
Ca2+ transient frequency (mHz)
ns
k
Ca2+ transient event duration (s)
l
m
Ca2+ synchronous burst amplitude (ΔF/F)
**
n
Ca2+ synchronous burst frequency (mHz)
o
Ca2+ synchronous burst event duration (s)

Figure 3: Species-specific differences in cytoplasmic calcium influx at stage-matched timepoints during spontaneous and synchronous activity a. Axon tract of a human (day 69) brain organoid slice in micropatterned devices expressing GCaMP7f. Zooms show representative timelapse of spontaneous calcium transients at different timepoints in individual axons, with ΔF/F0 fluorescent GCaMP7f intensity plots of axons in zooms. b. Axon tract of a mouse (day 15) brain organoid slice in micropatterned devices expressing GCaMP7f. Zooms show representative timelapse of spontaneous calcium transients at different timepoints in individual axons, with ΔF/F0 fluorescent GCaMP7f intensity plots of axons in zooms. c. Timelapses of an axon tract of a human (day 81) brain organoid slice in micropatterned devices expressing GCaMP7f, showing synchronous calcium activity, with ΔF/F0 fluorescent GCaMP7f intensity plots of axons indicated by arrowheads. d. Timelapses of an axon tract of a mouse (day 19) brain organoid slice in micropatterned devices expressing GCaMP7f, showing synchronous calcium activity, with ΔF/F0 fluorescent GCaMP7f intensity plots of axons indicated by arrowheads. e. Quantifications of the relative proportion of axon tract regions of human brain organoid slices in micropatterned devices exhibiting spontaneous or synchronised calcium activity at different timepoints. Day 62: n=6 regions of interest, Day 69: n=34, Day 76: n=29, Day 83: n=12. f. Quantifications of the relative proportion of axon tract regions of mouse brain organoid slices in micropatterned devices exhibiting spontaneous or synchronised calcium activity at different timepoints. Day 11: n=7 regions of interest, Day 13: n=21, Day 15: n=16, Day 18: n=6, Day 20: n=10, Day 24: n=3. g. Schematic of timepoints of developmental milestones in human and mouse brain organoids, indicating day 17 in mouse and day 76 in human as stage-matched timepoints based on data shown in Figure 3f and Supplementary Figure 4b-k. h. GCaMP7f intensity plots of axons of a human (day 69) and a mouse (day 15) brain organoid slice culture in micropatterned devices at stage-matched timepoints shown at the same scale. i. Quantifications of average mean amplitudes of spontaneous calcium transients at stage-matched timepoints in human (day 69) and mouse (day 15) brain organoid slice cultures in micropatterned devices expressing GCaMP7f. Human: n=151 axons, mouse n=50. j. Quantifications of average frequencies of spontaneous calcium transients at stage-matched timepoints in human (day 69) and mouse (day 15) brain organoid slice cultures in micropatterned devices expressing GCaMP7f. Human: n=151 axons, mouse n=50. k. Quantifications of average event durations of spontaneous calcium transients at stage-matched timepoints in human (day 69) and mouse (day 15) brain organoid slice cultures in micropatterned devices expressing GCaMP7f. Human: n=151 axons, mouse n=50. l. GCaMP7f intensity plots of axons of a human (day 82) and a mouse (day 19) brain organoid slice culture in micropatterned devices at stage-matched timepoints shown at the same scale. m. Quantifications of average mean amplitudes of synchronous calcium bursts at stage-matched timepoints in human (day 82) and mouse (day 19) brain organoid slice cultures in micropatterned devices expressing GCaMP7f. Human: n=23 regions of interest (average of 3 axons per ROI), mouse n=14. n. Quantifications of average frequencies of synchronous calcium bursts at stage-matched timepoints in human (day 82) and mouse (day 19) brain organoid slice cultures in micropatterned devices expressing GCaMP7f. Human: n=23 regions of interest (average of 3 axons per ROI), mouse n=14. o. Quantifications of average event durations of synchronous calcium bursts at stage-matched timepoints in human (day 82) and mouse (day 19) brain organoid slice cultures in micropatterned devices expressing GCaMP7f. Human: n=23 regions of interest (average of 3 axons per ROI), mouse n=14. All data are shown as mean ± SEM; *ns* $P > 0.05$, ** $P < 0.1$, **** $P < 0.0001$ as determined by unpaired *t* tests.

L-type VGCC-mediated calcium influxes modulate developmental tempo and axon tract length

Next, we sought to investigate if calcium dynamics could be sufficient to set developmental tempo in a manner leading to species-specific differences in axon tract length. To address

this, we aimed to identify the calcium channel(s) responsible for mediating the relevant calcium dynamics during these neuronal development stages. Our scRNA-seq analysis revealed an early onset of expression of calcium channels that localize to plasma membranes in both human and mouse neurons. Additionally, the observed calcium dynamics—characterized by spikes typically resulting from extracellular calcium influx through plasma membrane-localized channels rather than release from intracellular calcium stores that typically lead to calcium waves —suggests these calcium channels could be responsible[40,41]. Moreover, the long duration of the observed calcium transients, lasting several seconds, pointed to calcium channels with a slow inactivation rate, which is typical for the L-Type VGCCs[49], one of the channel types we found to have an early onset expression profile in our scRNA-seq. We therefore tested the effects of treatment with an L-Type VGCC antagonist, which blocked nearly all calcium dynamics in early stages corresponding with spontaneous activity, as well as during later stages corresponding with synchronous activity, and could be recovered upon washout (Figs 4a,b, Supplementary Fig 5a, Supplementary videos 5-10). Instead, treatment with an L-type VGCC agonist led to decreased frequencies with no difference in event duration or number of axons firing and, most notably, a profound increase in calcium amplitudes, similar to those observed in mouse organoids (Figs 4a-e).

We then examined the effect of these perturbations on human axon length, to test whether increasing, to mimic mouse dynamics, or decreasing calcium dynamics could influence tract length. We observed that potentiation of calcium amplitude did not affect axon outgrowth rates, with similar axon lengths observed after 7 days, but similar to mouse led to a shorter axonogenesis time window, resulting in shorter axon tracts (Figs. 4f-h). On the other hand, blocking L-type VGCC-mediated calcium influxes resulted in a longer axon outgrowth time window leading to an increase in axon tract length, beyond the unperturbed human axons (Fig. 4f,g).

In mature neurons, the relatively long-lasting calcium influxes mediated by L-type VGCCs typically lead to modulatory responses, aligning with our findings of long-term effects on the duration of axon tract developmental rather than on axon tract outgrowth rates. An important pathway for these modulatory responses involves the downstream increase of cAMP upon L-Type VGCC-mediated calcium influxes, with cAMP in turn also regulating L-Type VGCC activity, which has been linked to numerous neuronal developmental and plasticity processes, typically involving gene expression[50–53]. We therefore tested whether cAMP similarly impacted axon tract growth length and timing. When treating brain organoids undergoing axon tract development with cAMP, we observed shorter axon tracts and a shorter axon tract outgrowth duration, with no changes in axon tract outgrowth rates whilst in their elongation stage, thus

phenocopying the effects observed with an increased calcium influx and mimicking the mouse phenotype (Fig 4e,i,j). Together these data show that human axons, compared to those of mice, exhibit decreased calcium influxes, which underlie an extended time window of the axon tract outgrowth stage leading to an increase in axon tract length (Fig. 4k).

Figure 4

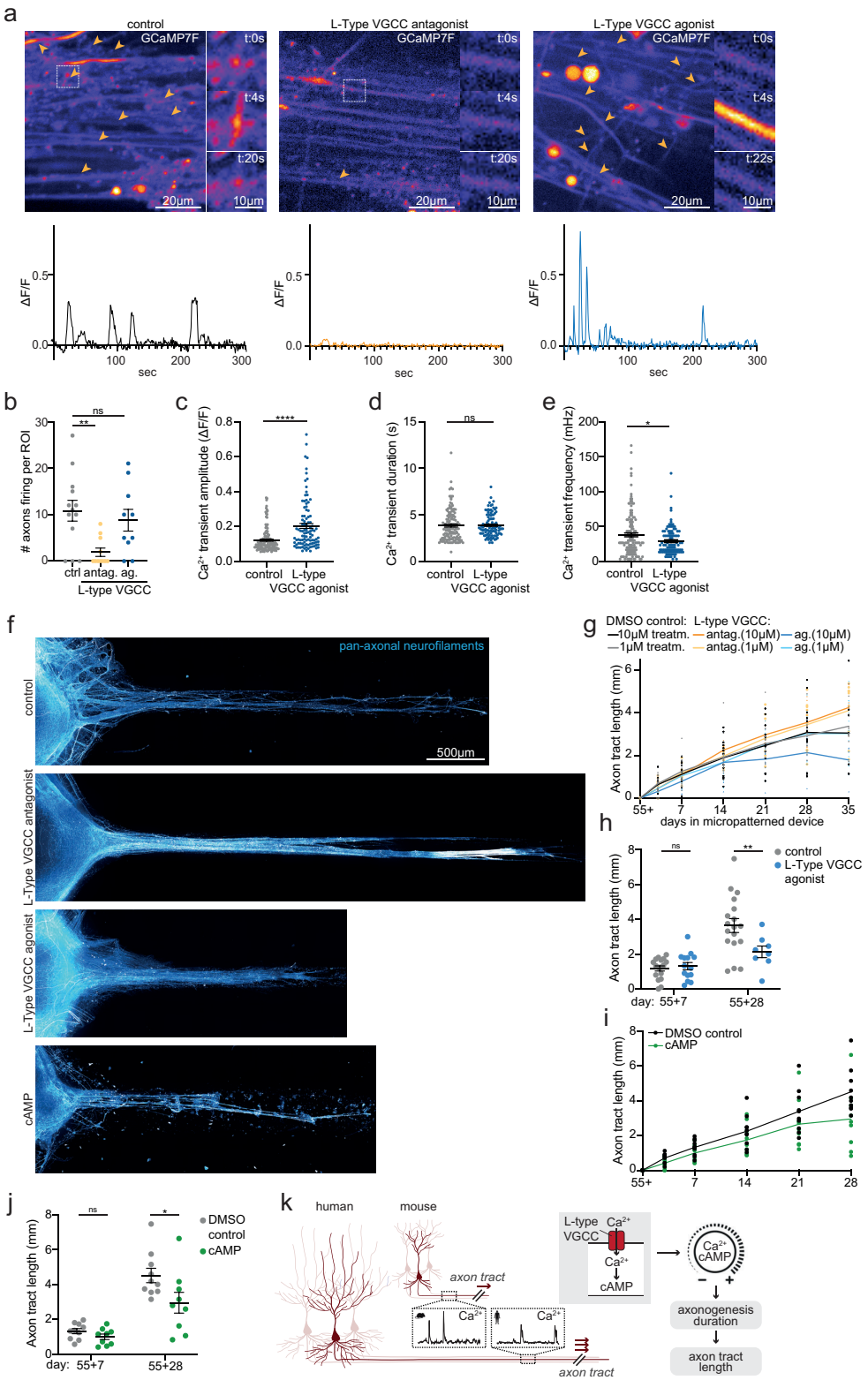

Figure 4: L-type VGCC-mediated calcium dynamics control the duration of the axonogenesis time window and axon tract length a. Axon tract of human (day 70) brain organoid slices in micropatterned devices expressing GCaMP7f and treated with DMSO (control), nimodipine (L-Type VGCC antagonist) or BayK8644 (L-Type VGCC agonist). Arrowheads mark axons showing calcium activity in a five minute timelapse, indicating nearly complete perturbation of calcium dynamics upon L-Type VGCC blockage. Zooms show representative timelapse of individual axons, with ΔF/F0 fluorescent GCaMP7f intensity plots of axons in zooms, showing the increase in calcium dynamics upon L-Type VGCC activation. b. Quantifications of number of axons firing in an ROI during a five minutes timelapse in axon tracts of human brain organoid slices (day 70) in micropatterned devices expressing GCaMP7f and treated with DMSO (control), nimodipine (L-Type VGCC antagonist) or BayK8644 (L-Type VGCC agonist). Control: n=13 regions of interest, L-Type VGCC antagonist: n=11, L-Type VGCC agonist: n=10. c. Quantifications of average mean amplitudes of spontaneous calcium transients in human brain organoid slice cultures (day 70) in micropatterned devices expressing GCaMP7f and treated with DMSO (control) or BayK8644 (L-Type VGCC agonist). Control: n=137 axons, L-Type VGCC agonist: n=100. d. Quantifications of average frequencies of spontaneous calcium transients in human brain organoid slice cultures (day 70) in micropatterned devices expressing GCaMP7f and treated with DMSO (control) or BayK8644 (L-Type VGCC agonist). Control: n=137 axons, L-Type VGCC agonist: n=100. e. Quantifications of average event durations of spontaneous calcium transients in human brain organoid slice cultures (day 70) in micropatterned devices expressing GCaMP7f and treated with DMSO (control) or BayK8644 (L-Type VGCC agonist). Control: n=137 axons, L-Type VGCC agonist: n=100. f. Representative images of axon tracts of human (day 90) brain organoid slices in micropatterned devices immunostained for pan-axonal neurofilaments and treated with DMSO (control), nimodipine (L-Type VGCC antagonist), BayK8644 (L-Type VGCC agonist), or cAMP. g. Quantifications of axon tract length of human brain organoid slice cultures in micropatterned devices, treated with DMSO (control), nimodipine (L-Type VGCC antagonist) or BayK8644 (L-Type VGCC agonist), at different timepoints. n=8-32 organoids. h. Quantifications of axon tract length of human brain organoid slice cultures in micropatterned devices, treated with DMSO (control) or BayK8644 (L-Type VGCC agonist), at day 55+7 and 55+28. Control: n=15 organoids (55+7) and n=14 (55+28), L-Type VGCC agonist: n=11 (55+7) and n=8 (55+28). i. Quantifications of axon tract length of human brain organoid slice cultures in micropatterned devices, treated with DMSO (control) or cAMP, at different timepoints. n=4-5 organoids. j. Quantifications of axon tract length of human brain organoid slice cultures in micropatterned devices, treated with DMSO (control) or cAMP, at day 55+7 and 55+28. Control: n=10 organoids (55+7) and n=10 (55+28), cAMP: n=9 (55+7) and n=9 (55+28). k. Schematic of model. Increase of L-type VGCC-mediated calcium, and downstream cAMP, levels accelerate developmental tempo during axonogenesis, resulting in shorter axon tract lengths. treatm., treatment. antag., antagonist. ag., agonist. All data are shown as mean ± SEM; $^{**}P < 0.1$, $^{****}P < 0.0001$ as determined by unpaired *t* tests.

DISCUSSION

We demonstrate a causal link between species-specific developmental tempo and structural neuronal complexity, specifically axon length, pointing to tempo modulation as an evolutionary mechanism allowing neurons with distinct species-specific complexities to develop. Assessing neuron development tempo usually involves comparing hallmarks of neuronal maturation at similar timepoints after inducing perturbations. Using this approach, tempo mechanisms have been identified that demonstrate an increase in dendritic length and synapse number upon acceleration of tempo[24,54,55], thereby deviating from the evolutionary pattern of slow tempo

linked with increased neuron complexity. It is unknown, and an interesting direction for future research, if these mechanisms would be consistent with evolutionary neuron complexities if developmental endpoints were measured, or if these instead describe molecular mechanisms for neurite outgrowth and synapse formation rates that may also exhibit differences in timing but are not the basis of evolutionary differences in complexity.

Here we assessed the link between the duration of a developmental stage, axon tract outgrowth, and the evolutionary morphological outcome, axon tract length. Focusing on this stage enabled the assessment of the complete developmental process within a realistic timeframe of weeks/months instead of years. To address this, we made use of modified human and mouse brain organoid slice cultures that are capable of forming self-organised axon tracts, and combined these with tailored micropatterned devices. Notably, in rare instances, axons did not form tract bundles, thus reflecting 2D-like neuron cultures, which coincided with a delay or absence of the onset of synchronous activity, as well as an increase in axon degeneration. This observation, along with emerging evidence of distinct axon outgrowth behaviours in 3D versus 2D environments, underscores the importance of studying axon development within more physiologically relevant axon bundles[56]. Thus, the methodologies described here allowed for the investigation of axon tract development within a more physiological environment than 2D cultures and, by using unguided protocols to generate brain organoids, resembling *in vivo*-like developmental timing. These methods were used to mechanistically explore the link between developmental tempo and evolutionary neuronal complexity.

We identified the intracellular tuning of calcium and cAMP levels as a mechanism to set developmental tempo, with species-specific differences in calcium levels not only unfolding at a different pace but also being quantitatively different at matched stages. Because of the ubiquitous processes acting downstream of calcium and cAMP, regulating these intracellular levels may serve as an effective means for evolution where small changes lead to substantial, and coordinated effects. Given the well-described role of calcium and cAMP dynamics on gene expression, particularly in the context of synaptic plasticity in mature neurons, it would be interesting to direct future research towards investigating how calcium in this context may influence relevant genetic developmental programs[57–60]. Spontaneous calcium transients have also been described to mediate cytoskeletal remodelling, thereby controlling transient processes such as axon turning and growth cone pausing[42,45,46,48]. These could similarly be involved in evolutionary differences, but may be more relevant for differences in actual growth rates, such as the faster initial outgrowth rate seen in mouse, rather than the differences in the duration of the stage. The long-term nature of the observed effects, together with the relatively long duration of calcium transients lasting several seconds, which typically have

more modulatory roles involving changes in gene expression and epigenetic remodelling, instead point to a potential cumulative effect of increased calcium and cAMP levels in setting the pace of the transition of neurodevelopmental processes.

The scRNA-seq data pointed to a pattern of calcium channels expressed throughout neuron development, suggesting a potential role of calcium levels in regulating tempo of not only axonogenesis, but also other neuron developmental processes. Consistent with this, calcium activity has been found to be involved in many processes of neuron development and plasticity, with perturbations of calcium dynamics affecting neurogenesis, axon pathfinding as well as regeneration, synapse formation and synaptic plasticity[25,39–48]. In the context of axonogenesis, whilst calcium dynamics have not yet been linked to evolutionary timing, perturbations have similarly been found to affect axon outgrowth, with increased neuronal activity or calcium dynamics leading to shorter and mistargeted axons, consistent with these findings[61,62]. Moverover, impairments in calcium dynamics have been linked to various neurodevelopmental disorders, including epilepsy, intellectual disability and autism spectrum disorder[63–66]. Notably, Timothy syndrome is specifically associated with gain-of-function mutations in L-Type VGCCs resulting in increased calcium influx, and this dysregulation is linked to cognitive impairments and, intriguingly, microcephaly—smaller brain size—which aligns with our observations of shorter axons upon L-Type VGCC activation[67,68]. Thus, the widespread role of calcium activity throughout neuronal development, together with these findings on its influence on developmental tempo, hint at a broader regulatory function of calcium dynamics in coordinating the tempo of these processes.

Evolutionary mechanisms ultimately stem from genetic differences. It would be interesting to direct future research at identifying the genetic changes responsible for species-specific differences in calcium dynamics. The reported species-specific differences in L-type VGCC-mediated calcium amplitudes may reflect variations in receptor levels at the plasma membrane, suggesting that genetic changes could affect expression levels, receptor targeting to plasma membranes or their turnover. As we observed a common signature of calcium-permeable ion channels with an early expression onset, an interesting avenue would be to explore the effect on tempo of other channels, such as NMDA receptors that were recently identified to exhibit calcium-mediated roles in synapse and dendrite formation[39]. Finally, as is common in evolution, a calcium and cAMP-mediated mechanism of timing is likely not a new innovation of the human lineage, and indeed, oscillatory cAMP signalling was recently described to act as a developmental timer in the amoeba species *D. Discoideum*[69]. Given this early emergence in evolution, as well as the appearance of calcium dynamics and ubiquitous

roles of cAMP across cell types and species, it would be interesting to explore if this timing mechanism also drives other developmental processes.

MATERIAL & METHODS

Cell lines

The human H9 (WA09, female) and H1 (WA01, male) embryonic stem cell lines were purchased from WiCell. The mouse E14 embryonic stem cell line (ESCs; RRID: CVCL_C320) was kindly gifted by the group of Marta Shahbazi. The U.K. Stem Cell Bank Steering and the ERC ethics committee has approved the use of human embryonic stem cells for this project, and the cell lines are registered on the Human Pluripotent StemCell Registry (hpscreg.eu). Human embryonic stem cells were maintained in StemFlex (Thermo Fisher Scientific, A3349401). Unless specified otherwise, human organoids were generated from H9 stem cells. E14 embryonic mouse stem cells were expanded in 2iLIF media and transferred to StemFlex supplemented with 1000 U ESGRO recombinant mouse leukemia inhibitory factor (mLIF; Sigma-Aldrich #ESG1107) before generation of organoids using the same protocol as for human, as described [27]. All stem cell lines were kept as feeder-free cultures on plates coated with growth factor reduced Matrigel (Corning #356230) and passaged about 2x a week using EDTA. For establishment of the mCherry-expressing H1 and E14 lines, annotated as H1 PB001 and E14 PB001, plasmids PB001 carrying the mCherry cassette and pBase carrying the transposase (2 µg of each plasmid) were electroporated into 10 million H1 or E14 cells using the Human Stem Cell Nucleofector Kit 1 (Lonza, VPH-5012). Following electroporation, cells were grown in one well of a 6-well plate in StemFlex supplemented with 1 nM ROCK inhibitor (BD Biosciences, 562822). After 48 hours post electroporation, the cells were selected using StemFlex supplemented with Puromycin (Gibco, A11138-03) at a final concentration of 0.5 µg/mL.

Plasmids

The pGP-AAV-syn-jGCaMP7f-WPRE plasmid was obtained from Douglas Kim and the GENIE project (Addgene, 104488) [70]. The MARCKS-GFP plasmid was obtained from the group of Casper Hoogenraad, with the cassette composed of the first 41 amino acids of the MARCKS protein containing an Alanine to Cysteine mutation (MGCQFSKTAAKGEAAAERPGEAAVASSPSKANGQENGHVKV), fused to a GS linker and TagRFP-T [71]. The PB001 insertion plasmid contained the insert encoding human ubiquitin promoter driving expression of mCherry followed by P2A ribosome skipping sequence and puromycin resistance cassette, with bGH polyA termination signal, flanked by PB transposase inverted terminal repeat sequences.

Human and mouse brain organoid cultures

Human and mouse cerebral organoids were generated, with some modifications, as described before, following the same protocol steps with the timing of each step tailored to match their species-specific developmental tempo [27,37,72]. Briefly, on day 0, human or mouse embryonic stem cells were dissociated with Accutase (Gibco, A1110501), resuspended in EB Formation medium (StemCell Technologies, 8570) supplemented with 50 µM ROCK inhibitor Y27632 (SantaCruz Biotechnology, sc-281642A) and 4000 cells per well were seeded into ultra-low attachment U-bottom 96-well plates (Corning, 7007) to form embryoid bodies. On day 5 for human or day 2 for mouse, the media was replaced with Neural Induction medium (StemCell Technologies, 8570). On day 7 for human or day 5 for mouse, embryoid bodies were embedded in Matrigel (Corning, 354234) and transferred to 6-well plates with Expansion medium (StemCell Technologies, 8570). On day 10 for human and day 6 for mouse, the culture media was replaced with Improved Differentiation Medium without vitamin A (IDM-A: 1:1 [v/v] DMEM/F12 (Gibco, 11330032) and Neurobasal (Gibco, 21103049) media, 1:200 [v/v] N-2 supplement (Gibco, 7502048), 1:50 [v/v] B-27 supplement minus vitamin A (Gibco, 12587010), 1x GlutaMAX (Gibco, 35050038), 0.5x MEM non-essential amino acid solution (MEM-NEAA; Gibco, M7145), 2.5 µg/mL human insulin (Sigma-Aldrich, I9278), 50 µM 2-mercaptoethanol (Gibco, 31350010), 1:100 [v/v] penicillin-streptomycin (Gibco, 15140122)). On day 14 for human and day 7 for mouse, Matrigel was removed from the organoids, by either manual dissection or chemical Matrigel removal. For the latter, the bulk of Matrigel was initially removed by manual dissection, after which organoids were transferred to a dish, covered with cell recovery solution (Corning #354253) and incubated at 4°C for 20 min with regular gentle agitation to mix. Cell recovery solution was removed and organoids were gently washed thrice with phosphate-buffered saline (PBS; 125 mM NaCl, 17 mM Na_2HPO_4, 9 mM NaH_2PO4, pH 7.4). Organoids were kept on an orbital shaker (57 RPM, 25 cm orbit) and cultured in 5 cm dishes in IDM-A medium until day 30 for human and day 8 for mouse, and then in IDM-A medium supplemented with 1:50 [v/v] Matrigel until ready for slicing.

Human and mouse brain organoid slice cultures

Human and mouse brain organoids were sliced similarly to previously described, with some modifications [28]. In brief, unless stated differently, mouse and human organoids were harvested on respectively day 8 and 55. Organoids were embedded in 3% low-gelling temperature agarose (Sigma, A9414) in molds (Sigma, #E6032), incubated on ice for 30-60 min, and sections with 300 µm thickness were collected using a Leica VT1000S vibrating microtome. Organoids were sliced and kept as ALI-COs or transferred to micropatterned devices for axon outgrowth experiments. For ALI-CO cultures, slices were cultured on Millicell-CM culture inserts (Millipore, #PICM0RG50). For axon tract outgrowth assays, slices were

transferred to micropatterned devices as described below. Brain organoid slice cultures were kept in serum-free slice culture medium (SFSCM; Neurobasal (Invitrogen, #21103049), 1:50 (v/v) B27+A (Invitrogen, cat. #17504044), 1X (v/v) Glutamax (Gibco #35050038), 1:100 [v/v] penicillin-streptomycin (Gibco), 1:500 (v/v) Fungin (Invivogen, #ant-fn)). After 14 days for human and 3 days for mouse, and every 3-4 days after, ~50% of the medium was replaced with BrainPhys medium (BP; BrainPhys Neuronal Medium N2-A SM1 kit (StemcellTechnologies, #05793), 1:100 [v/v] penicillin-streptomycin (Gibco), 1:500 (v/v) Fungin (Invivogen, #ant-fn)).

Transplantation experiments

H1 PB001 human and E14 PB001 mouse ALI-COs were collected on respectively day 59 and days 9-12, washed once in PBS. Tissues were homogenised by gently resuspending 3-5x in 200 µl Accumax solution (Merck, A7089), followed by a 15 min incubation at 37°C on a shaker (57 RPM, 25 cm orbit), with gentle mixing after every 5 min. The cell suspension was further homogenised by gently resuspended another 3-5x and kept on ice to stop enzymatic reactions. If there was undissolved tissue, the cell suspension was filtered through a 70 µm strainer. Cells were counted, pelleted (200 *g*, 4 min), resuspended in 10 µl SFSCM and 2-6K cells were added dropwise on top of human (days 59-120) or mouse (day 12) ALI-COs.

Fabrication of micropatterned devices

Microfluidic devices were produced by replica molding using polydimethylsiloxane (PDMS, Sylgard 184; Ellsworth Adhesives, Wilmington, MA, USA) on a master mold that was fabricated on a silicon wafer using soft lithography [73,74,75,76]. The master mold was fabricated to 450 µm thickness using SU8-100 photoresist according to the manufacturer's (Kayaku® Advanced Materials) instructions and the OAI Model 204 Mask Aligner for UV exposure (Supplementary Fig 2A). The dimensions and surface characterization of the master mold are shown in Supplementary Fig 2C. Next, the PDMS pre-polymer and curing agent were mixed in a 10:1 weight ratio to make PDMS and then degassed in a desiccator before pouring onto the master mold. The PDMS was cured at 65°C for 8 hr (Supplementary Fig 2B). After curing, milli-wells were punched using a 3 mm biopsy puncher. Micropatterned devices were then soaked in ethanol, placed onto the glass bottoms of either 35 mm dishes (World Precision Instruments, D35-100) for live-imaging experiments, or 24-well plates (Cellvis, P24-0-N) or 12-well plates (Cellvis, P12-1.5H-N), and kept in the hood overnight, allowing evaporation of ethanol and subsequent bonding.

Brain organoid slice cultures in micropatterned devices and drug treatments

The chambers and channels of the micropatterned devices were coated with 0.5 mg/mL growth factor reduced Matrigel (Corning, 356230) in DMEM/F12 for at least 1h at 37°C/5%CO_2. Right before placing brain organoid slices (generated as described above) in the micropatterned devices, Matrigel coating was removed, and brain organoid slices were gently placed in the chambers before the opening of the channel. Any reminiscent liquid was removed and slices were kept at 37°C/5%CO_2 for 30 min-1h after which SFSCM medium was added. Subsequent medium changes were similar to the ALI-CO cultures. For drug treatments, one day after brain organoid slices were placed in the devices, and during subsequent medium changes, medium was replaced with SFSCM or BrainPhys (at similar timepoints as with ALI-CO cultures described above) supplemented with indicated final concentrations of either 1 µM or 10 µM BayK8644 (Stratech Scientific, S7924-SEL), 1 µM or 10 µM Nimodipine (Selleckchem, S1747) or 100 µM 8-Br-cAMP (BioLog, B007). For the wash-out experiment in Supplementary Fig 5a, floating brain organoid slices were incubated with BrainPhys supplemented with 10 µM Nimodipine (Selleckchem, S1747) for 1h and kept on an orbital shaker (57 RPM, 25 cm orbit). After timelapse acquisitions, medium was replaced with BrainPhys and slices were placed back on the shaker for 3h for the wash out experiment, followed by another series of timelapse acquisitions.

Mouse spinal cord explant co-culture in micropatterned devices

Mouse tissue was collected in accordance with the UK Animals (Scientific Procedures) Act 1986 and European Community Council Directive on Animal Care by a trained technician of the MRC-LMB animal facilities. Mouse spinal cord explants from C57BL/6 E12.5 embryos were obtained as described before [28]. In brief, mouse uteruses and subsequently dissected embryos were handled in ice-cold HBSS without Calcium and Magnesium (Gibco, 14175095) and kept over ice throughout the handling process. Using microdissection equipment, embryos were excised and liberated from the uterine horns, before being pinned down supine through their limbs for stability. The dorsal skin, meninges, and vasculature were peeled away from the back using fine tweezers to expose the spinal cord in the midline. Cuts were made 1 mm laterally down each side of the spinal cord, to free it from the sides of the body. Subsequently, the excised spinal cord and surrounding tissue was turned on its side so that the viscera could be removed from its ventral aspect, leaving just the spinal cord and some associated paraspinal muscle around it. The tail and head were removed from each respective end. The dissected mouse spinal cords were then prepared as for organoid slice cultures, and sections were placed in the channel of the micropatterned devices opposite the organoid slice.

Viral emGFP, MARCKS-GFP and GCaMP7f labelling

For sparse labelling of cells enabling assessing cell morphologies, ALI-COs were induced with 0.05 - 0.5 µl Sendai virus carrying emGFP (ThermoFisher, A16519) that was diluted in 2 µl SFSCM for mouse ALI-COs or 10 µl SFSCM for human ALI-COs and added dropwise onto the slice. For MARCKS-GFP labelling of human brain organoid slices in co-culture with mouse spinal cord explant, human brain organoid slices in micropatterned devices were induced with lentivirus carrying doxycycline-induced MARCKS-GFP, generated as described in [71], ~1-3h after being placed in the devices. For viral induction, medium was removed, and virus diluted in 10 µl SFSCM was added to the chamber, after 30 min - 1h a total of 2 ml SFSCM was added back again. The next day, slices were washed before mouse spinal cord explants were placed on the opposing chambers of the devices to ensure specific labelling of human organoids only. For calcium imaging, brain organoids in micropatterned devices were induced with AAV1 virus carrying GCaMP7f (Addgene, 104488), similar as described above with MARCKS-GFP induction, within 3-36h after organoids were placed in the micropatterned devices. Calcium imaging was performed at least 7 days after viral induction to ensure sufficient GCaMP7f expression.

Fixation, cryosectioning and immunostaining

At indicated timepoints, ALI-COs were fixed overnight at 4 °C with 4% [v/v] paraformaldehyde in phosphate buffer (145 mM Na_2HPO_4, 21 mM NaH_2PO_4, pH 7.4) and washed three times with PBS. For cryosectioned samples, slices were incubated in phosphate buffer with 30% [w/v] sucrose at 4°C overnight. Organoids were embedded in 7.5% [w/v] gelatin (Sigma-Aldrich, G1890), 30% sucrose in phosphate buffer, and the gelatin blocks were frozen by submersion in cold isopentane (-50 °C) for 90 s. Frozen blocks were stored at -80 °C until being sectioned in 20 µm slices by CM1950 cryostat (Leica Biosystems) and collected on charged slides (SuperFrost Plus Adhesion; Fisher Scientific, J1800AMNZ). Cryosections were incubated with primary antibodies overnight at 4°C, and secondary antibodies for 1h at room temperature, with 3x 10 min PBS wash steps after every antibody incubation. Whole ALI-COs were incubated with primary antibodies and secondary antibodies for 48 h at room temperature, with 3x 8 h washes after every antibody incubation. Primary and secondary antibodies were diluted in permeabilisation buffer (0.25% Triton-X, 4% donkey serum in PBS). The following primary antibodies were used in this study: Bassoon (Enzo Life Sciences, SAP7F407), GAPDH (Abcam, ab8245), GFAP (Abcam, ab7260), Homer1 (Synaptic systems, 16003), PSD95 (Abcam, ab18258), Pan-axonal neurofilaments Clone SMI312 (Biolegend, 837904), Synaptophysin (Abcam, ab32127), Trim46 (Synaptic Systems, 337003), VGAT (Synaptic Systems, 131003). Whole ALI-COs were mounted using Prolong Diamond (Invitrogen, P36970) with coverslips on microscope glass slides.

Immunoblotting

For sample collection, ALI-COs were cleared of residual agarose, washed three times in ice-cold PBS, snap-frozen, and stored at -80°C. Protein lysates were obtained by thawing samples on ice, homogenized by resuspending 20x with a Dounce homogenizer in 1 ml modified-RIPA (mRIPA: 1% Triton-X, 0.1% SDS, 150 mM NaCl, 50 mM Tris pH 7.4, 2 mM EDTA, 12 mM sodium deoxycholate) supplemented with protease inhibitors (Thermo Fisher, 78430), followed by a 40 min incubation at 4°C on a rotor. Protein lysates were centrifuged (20,000 *g*, 20 min, 4°C) and protein concentrations were obtained using Quick Start Bradford Dye Reagent (Bio-Rad, 5000205). Normalized protein samples were resolved on 4-20% tris-glycine gels and transferred to Amersham Hybond P 0.45 PVDF blotting membranes (GE Healthcare, 10600023). Membranes were blocked for 1h at room temperature in PBS-T with 5% milk, incubated overnight at 4°C with primary antibodies diluted in PBS-T with 2% milk and for 1h at room temperature with secondary antibodies diluted in PBS-T with 2% milk, with three 10 min wash steps in PBS-T after every antibody incubation. Resolved proteins on the blots were visualised using a Gel Doc XR+ system.

Microscopy, live-imaging and image-analysis

Brightfield images of axon tracts growing in micropatterned devices and fluorescent images of the MARCKS-GFP-positive and mCherry-positive axon tracts for the co-culture experiments were acquired using an Evos XL Core microscope (Thermo Fisher Scientific). Images for synaptogenesis and gliogenesis were acquired on an inverted Zeiss LSM 880 Airyscan equipped with a 63x/1.4 NA Oil lens, and GaAsp, spectral and Airyscan detectors. For the synaptogenesis analysis, the super resolution settings of the Airyscan detectors were used to acquire high-resolution images. Confocal imaging of all other fixed samples was performed on an inverted Nikon CSU-W1 spinning-disk microscope, equipped with 10x/0.45 NA Air, 25x/1.05 NA Silicone Oil, 60x/1.2 NA Water lenses, sCMOS camera (95% QE). Displayed microscopy images represent a maximum intensity projection of a Z-stack covering the region of interest. Live-imaging of calcium dynamics was conducted on an inverted Nikon X1 Spinning Disk inverted microscope, containing a 60x/1.2NA Water lens, sCMOS cameras (95% QE), and a heated and gas-controlled incubation chamber. ALI-COs were kept at 37 °C and 5% CO2, and timelapses were acquired at a 1Hz imaging speed and single plane. Image processing and analysis was performed in Fiji.

Quantifications neuronal polarity, 3D neurite lengths and soma areas.

Neurons were categorised as polarised when one of the neurites, the future axon, was at least two-fold longer than the second longest neurite. To assess neurite lengths, a line was manually drawn to trace the neurite length, a Z-plot was generated and the length of the neurite

was traced to obtain 3D length measurements. Soma areas were obtained by manually tracing soma outlines.

Quantifications of axon tract lengths in micropatterned devices.

Brightfield images of the overlapping axon tract regions, covering the tract from beginning to end, were stitched using the Fiji plugin Pairwise Stitching (https://github.com/fiji/Stitching/blob/Stitching_-3.1.9/src/main/java/plugin/Stitching_Pairwise.java) [77]. Axon tract lengths were manually traced, using the surface of the organoid where the tract extends from as start and the most distal part of the tract as end.

Quantifications of proportion of spontaneous and synchronous calcium activity and stage-matching.

Timelapses with 133.62×133.62µm image size and 5 min durations were acquired from axon tract regions in micropatterned devices. If at least two axons showed a clear synchronous firing pattern during the acquisition, it was classified as synchronous calcium activity, otherwise as spontaneous calcium transients. Synchronous firing events first appeared on day 69 for human organoids and day 15 for mouse, during which the majority of the calcium activity events remained as non-synchronous spontaneous transients. At these matched timepoints, timelapses that did not exhibit any synchronous events were subjected to cross-species analysis of spontaneous calcium transients. Cross-species analysis of synchronous burst activity was conducted on day 82 in human and day 19 in mouse, marking the first timepoints at which the majority of calcium activity events exhibited synchrony. At these stages, robust burst activity was observed throughout the entire tract, whereas earlier timepoints showed that synchronous activity occasionally involved the coordinated firing of individual axons within the tract.

Calcium activity quantifications.

Regions of interest were manually delineated for each image. For spontaneous calcium activity measurements, all axons exhibiting calcium activity in each acquired 5 min timelapses were traced and analysed. For synchronous calcium burst activity, three axons were traced per timelapse, and their read-outs were averaged and treated as a single data point. The corresponding temporal signal for each ROI was subsequently analyzed using a custom-developed ImageJ macro (https://github.com/MRC-LMB-Light-Microscopy-Facility/imagej-macro-calcium-imaging; DOI: 10.5281/zenodo.14562107). Briefly, the temporal signal was derived by calculating the mean pixel intensity within each ROI at each time point. To mitigate noise, the raw signal underwent sequential temporal filtering, employing a median filter followed by a minimum filter. Putative events were identified by detecting local maxima in the ratio exceeding a pre-defined threshold. Onset and offset times for each event were defined by contiguous temporal segments exceeding this threshold and containing a single local

maximum. The spatiotemporal characteristics of each identified event, specifically its location and maximum amplitude, were recorded and subsequently aggregated for each ROI in order to compute mean amplitude and frequency. The ΔF/F traces were obtained using a sliding window of 21 frames. Calcium signals above a 0.045 threshold were identified as transients and their mean amplitudes, event frequencies and event durations were analysed.

Glia cell proportion quantifications.

Images with a 66.10×66.10×1.5 µm volume of brain organoid cryosections immunostained for DAPI and GFAP were acquired, with regions selected using the DAPI channel to ensure blinded analysis. Nuclei numbers from a maximum intensity projection were assessed using the Fiji plugins Watershed Separation (https://github.com/imagej/ImageJ/blob/v1.54f/ij/plugin/filter/EDM.java) and Particle Analyzer (https://github.com/imagej/ImageJ/blob/v1.54f/ij/plugin/filter/ParticleAnalyzer.java), and classified as GFAP-positive or GFAP-negative cells to calculate proportions.

Synapse quantifications.

Images with a 19.44×19.44×1.35 µm volume of brain organoid cryosections immunostained for DAPI, Bassoon and PSD95 were acquired, with regions selected using the DAPI channel to ensure blinded analysis. Synaptic structures were identified by co-localisation of Bassoon and PSD95 using a custom-developed ImageJ macro (https://github.com/MRC-LMB-Light-Microscopy-Facility/imagej-macro-cytoplasmic-3d-spot-overlap
DOI: 10.5281/zenodo.14562113), with synapse numbers normalised to image volumes.

Single cell RNA sequencing

At indicated days, a total of 48 human and 24 mouse samples were collected for single cell RNA sequencing, with 3 ALI-COs from two independent batches per timepoint. ALI-COs were collected using a cut p1000 tip, transferred to a 15 ml tube pre-coated with BSA and washed once with PBS. Accumax solution (Merck, A7089), 1 ml for human and 200 µl for mouse, was added to the ALI-COs, tissues were gently resuspended 3-5x using a p1000 tip to break it up in smaller pieces, followed by a 15 min incubation at 37°C on a shaker (57 RPM, 25 cm orbit), with gentle mixing after every 5 min. The enzymatic activity was stopped by adding 1:10 Fetal Bovine Serum (FBS; Merck #F2442), the cell suspension was gently resuspended another 3-5x and placed on ice to further halt enzymatic reactions. The cell solution was filtered through a 70 µm strainer, centrifuged (300 *g*, 10 min, 4°C) and resuspended in cell prefixation buffer (Parse Biosciences). Sample fixation and library preparation were performed following the Evercode v3 Parse Biosciences protocol. Mouse and human samples were combined and demultiplexed during subsequent bioinformatic analysis. For species demultiplexing, raw reads were aligned to a combined Human (GRCh38) and Mouse reference (GRCm39) using Split Pipeline v1.0.3 provided by Parse Biosciences. Mapping rates for transcripts to each

species reference genome were calculated for each cell based on the obtained counts matrix. Species were demultiplexed by comparing the mapping rates and assigned as the species of the higher mapping rate genome. Further, the cell barcodes of human and mouse assigned cells were extracted and used to subset counts matrices obtained by aligning the raw reads to human and mouse genomes separately. These counts matrices were treated separately through the following analysis steps. For quality control and normalisation, cells with high mitochondrial UMI fractions were excluded as that is a known indication of cell stress. Next, the filtered count matrix was passed to 'basicP2proc' for filtering based on minimum cells expressing a gene (10) and minimum transcript number per cell (1000), variance normalisation, and dimensionality reduction by Principal Component Analysis (PCA) based on top 2000 most highly variable genes yielding 30 principal components. Cell doublets were identified using scDblFinder from DropletUtils. Uniform Manifold Approximation and Projection (UMAP) were obtained based on these for better data visualisation. Assessment of batch effects led us to apply the Harmony integration method on the PCAs [78]. The new UMAP representation was calculated on batch-integrated PCs to visualise the transcriptional landscape. Then, cells were pre-clustered based on K-Nearest Neighbour graph using pagoda2 function 'getKnnClusters'. Initial cluster annotations were performed manually based on the localisation of known marker expressions.

Statistical analysis

Statistical details are included in corresponding figure legends. *P*-values are annotated as follows: ns $P > 0.05$, $*P < 0.05$, $**P < 0.01$, $***P < 0.001$ and $****P < 0.0001$. Data processing and statistical analysis were conducted in Prism GraphPad (version 10.0) software.

ACKNOWLEDGEMENTS

The authors would like to thank members of the Lancaster lab for helpful feedback and discussions. We also thank Jess L. Sevetson and Alex Justin for their support with bioengineering the micropatterned devices. Thanks to Marta Shahbazi for providing the mouse E14 cell line and to Casper Hoogenraad for gifting the MARCKS-GFP plasmid. This work was supported by the Medical Research Council (MC_UP_1201/9) and the European Research Council (ERC-STG, 757710) to MAL. FWL is a non-stipendiary European Molecular Biology Organisation Postdoctoral Fellow (EMBO, ALTF 845-2021) and supported by the Netherlands Organisation for Scientific Research (NWO-Rubicon, 019.211EN.032ß).

AUTHOR CONTRIBUTIONS

FWL designed and performed experiments, analysed data and wrote the manuscript. HMS conducted and analysed data for the synaptogenesis experiments, under supervision of FWL,

and performed bioinformatic analysis. II-R and LG conducted initial bioinformatic analysis. KV, MM and JM generated master molds for micropatterned devices, under supervision of MT. NZG conducted and analysed data for the gliogenesis experiments, under supervision of FWL. DJLDS and MAL generated mouse spinal cord explant tissues and contributed to sample collection for RNA sequencing. MAL supervised the study and wrote the manuscript.

COMPETING INTERESTS

MAL is an inventor on patents covering cerebral organoids, and is co-founder and advisory board member of a:head bio.

Supplementary Figures

Supplementary Figure1

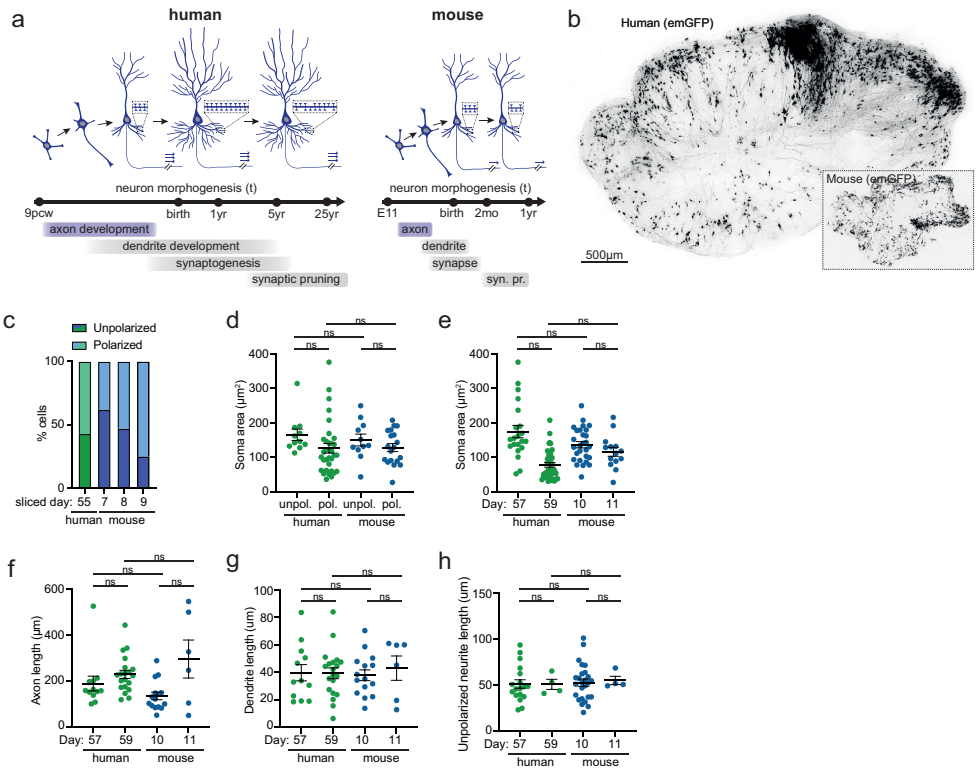

Supplementary Figure 1: Stage-matching of onset of axon formation and application of micropatterned devices to investigate subsequent axon tract elongation

a. Schematic illustration of the sequential developmental steps and timeline of human and mouse cortical neuron morphogenesis, with species-specific neuron morphologies drawn to scale [4–9,79–81].

b. Representative image of a day 69 human and a day 15 mouse ALI-CO with sparsely labelled emGFP-positive cells.

c. Quantifications of the relative proportion of sparsely labelled emGFP-positive unpolarized and polarized neurons 24-36 hours after slicing in human ALI-COs, sliced at day 55, and mouse ALI-COs, sliced at day 7, 8 or 9. Hm day 55: n=21 neurons, Ms day 7: n=22, Ms day 8: n=51, Ms day 9: n=8.

d. Quantifications of soma areas in sparsely labelled emGFP-positive unpolarised and polarised neurons on day 57 and 79 in human ALI-COs, and day 10 and 11 in mouse ALI-COs. Hm unpolarized: n=11 neurons, Hm polarized: n=32, Ms unpolarized: n=39, Ms polarized: n=48.

e. Quantifications of soma areas in sparsely labelled emGFP-positive unpolarised and polarised neurons in human (day 57-59) and mouse (day 10-11) ALI-COs. Hm day 57: n=21 neurons, Hm day 59: n=40, Ms day 10: n= 57, Ms day 11: n=14, Ms day 15: n=7.

f. Quantifications of 3D axon length in sparsely labelled emGFP-positive polarised neurons on day 57 and 79 in human ALI-COs, and day 10 and 11 in mouse ALI-COs. Hm day 57: n=12 neurons, Hm day 59: n=20, Ms day 10: n= 42, Ms day 11: n=6.

g. Quantifications of 3D length of the longest dendrite in sparsely labelled emGFP-positive polarised neurons on day 57 and 79 in human ALI-COs, and day 10 and 11 in mouse ALI-COs. Hm day 57: n=12 neurons, Hm day 59: n=20, Ms day 10: n= 42, Ms day 11: n=6.

h. Quantifications of 3D neurite length in sparsely labelled emGFP-positive unpolarised neurons on day 57 and 79 in human ALI-COs, and day 10 and 11 in mouse ALI-COs. Hm day 57: n=18 neurons, Hm day 59: n=4, Ms day 10: n= 74, Ms day 11: n=4.

All data are shown as mean ± SEM; *ns* $P > 0.05$ as determined by unpaired *t* tests.

Supplementary Figure 2

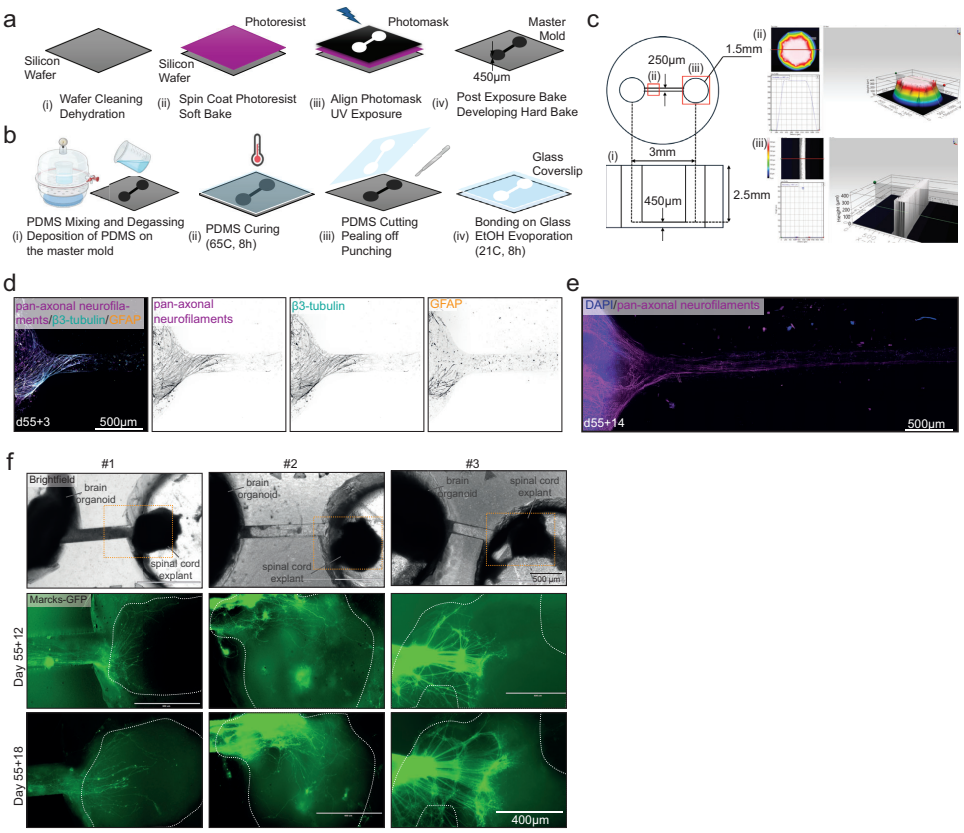

Supplementary Figure 2: Micropatterned device fabrication and application to investigate axon tract outgrowth

a. Photolithography process for master mold fabrication. (i) Wafer cleaning (15 min, Nanostrips® and 15min, DI water), dehydration (15 min, 150°C). (ii) Spin coat SU8-100 photoresist (Step 1: 500 rpm at 100 rpm/sec, 10 sec.

Step 2: 1000 rpm at 300 rpm/sec, 30 sec), soft bake photoresist (Step 1: 30 min, 65°C. Step 2: 90 min, 95°C). (iii) Prepare Mylar photomask (Step 1: CAD design and conversion. Step 2: order printing the CAD design), UV exposure at OAI Model 204 Mask Aligner (Step 1: align photomask and substrate. Step 2: UV exposure time 115.21 sec, channel intensity (mW/cm^2):7.2, exposure energy (mJ/cm^2): 829.5). iv. Post exposure bake (Step1: 1min, 65°C. Step 2: 20 min, 95°C), developing (Step 1: 20 min SU8 developer. IPA rinse, nitrogen dry. Step 2: hard bake, 15 min, 150°C).

b. Soft lithography process for PDMS microstructure fabrication. (i) PDMS mixing (10:1), degassing, and deposition onto fabricated master mold. (ii) PDMS curing (65°C for 8 hours). (iii) Cutting and peeling off the PDMS, punching the milli wells. (iv) Oxygen plasma exposure (30 sec) for bonding devices onto glass and placing onto a hot plate (80°C) for 45 min.

c. Device features. (i) 2D schematic of the microstructure master mold in top and side view with dimensions. (ii) Thickness characterization of the milli well. (iii) Thickness characterization of the master mold microchannel.

d. Human brain organoid slice cultures placed in the chambers at day 55, fixed 3 days later and immunostained for pan-axonal filaments, β3-tubulin and GFAP.

e. Human brain organoid slice cultures placed in the chambers at day 55, fixed 14 days later and immunostained for pan-axonal filaments and DAPI.

f. Brightfield images of micropatterned devices with a human organoid slice culture in the left chamber and a mouse spinal cord explant in the right chamber. Zoom shows Marcks-GFP-positive axons from a human brain organoid slice culture extending onto a mouse spinal cord explant, indicated by dashed line, 12 days and 18 days after being placed in the chamber (at day 55).

pcw, postconception week. yr, year. mo, months. syn. prun., synaptic pruning. Hm, human. Ms, mouse. All data are shown as mean ± SEM; ns $P > 0.05$, *$P < 0.05$, ****$P < 0.0001$ as determined by unpaired *t* test.

Supplementary Figure 3

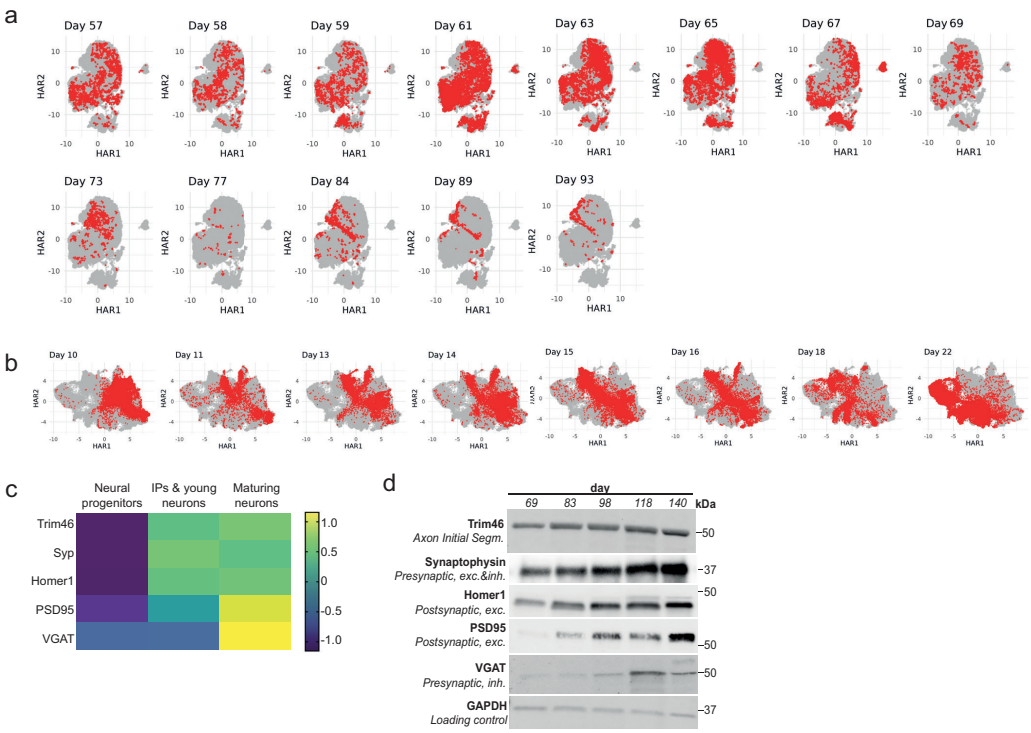

Supplementary Figure 3: In-depth analysis and quality control of single cell RNA sequencing of human and mouse ALI-COs

a. UMAP feature plots of human scRNA-seq for different timepoints.

b. UMAP feature plots of mouse scRNA-seq for different timepoints.

c. Heatmap of z-score of RNA expression of indicated neuron development genes in clusters of the human scRNA-seq (corresponding to clusters shown in Fig 1a).

d. Western blot of human ALI-COs at different timepoints showing temporal expression profiles of neuron maturation proteins (same markers as shown in c).

Supplementary Figure 4

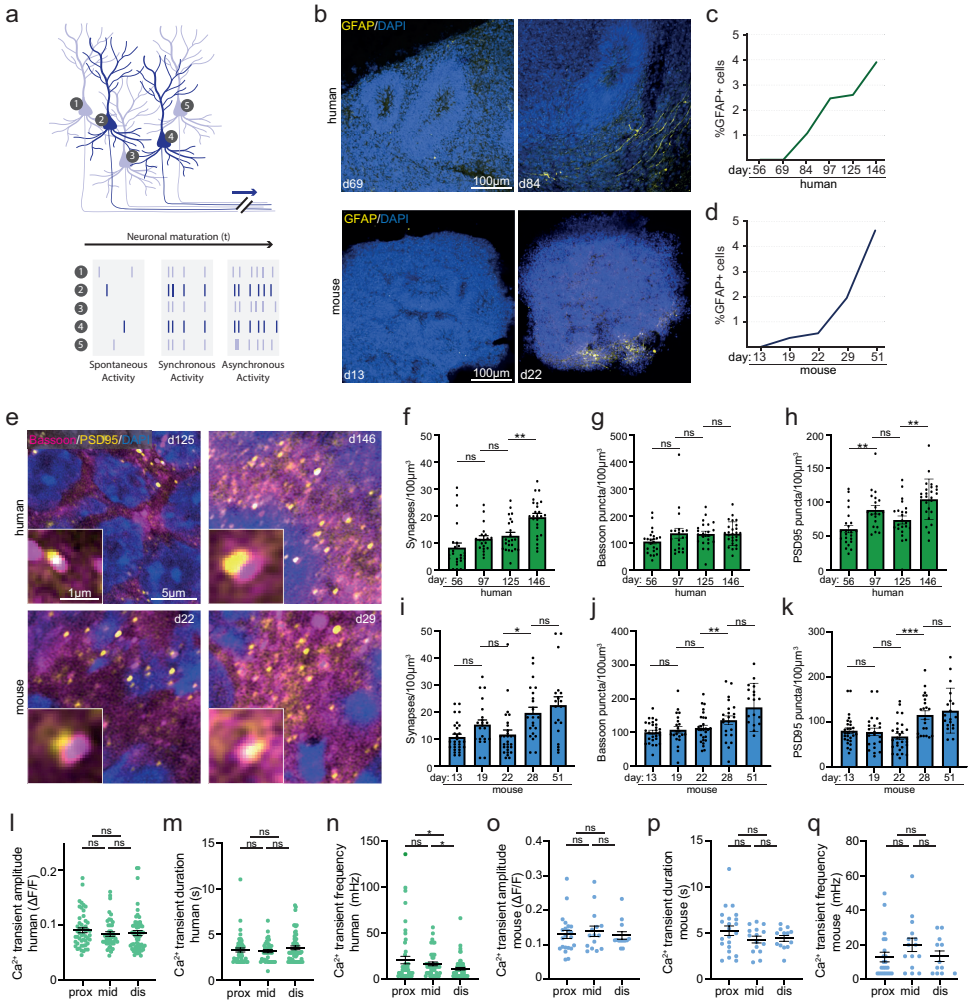

Supplementary Figure 4: Stage-matching onset of gliogenesis and increase of synaptogenesis in human and mouse

a. Schematic of different modes of neural activity during neuron development [82–84].

b. Representative images of cryosections of human and mouse ALI-COs at indicated days immunostained for GFAP and DAPI.

c. Quantifications of proportion of GFAP-positive cells in human ALI-COs across different timepoints. Day 56: n=14 regions of interest, Day 69: n=14, Day 84: n= 14, Day 97: n=13, Day 125: n=14, Day 14: n=13.

d. Quantifications of proportion of GFAP-positive cells in mouse ALI-COs across different timepoints. Day 13: n=14 regions of interest, Day 19: n=14, Day 22: n=14, Day 19: n=14, Day 42: n=9, Day 51: n=13.
e. Representative images of cryosections of human and mouse ALI-COs immunostained for bassoon, PSD95 and DAPI, showing an increase of synaptic puncta at indicated timepoints. Zoom represents a co-localisation of pre- and postsynaptic structure.
f. Quantifications of number of co-localising bassoon and PSD95 puncta in cryosections of human ALI-COs at different timepoints. Day 56: n=24 regions of interest, Day 69: n=13, Day 84: n=11, Day 97: n=19, Day 125: n=22, Day 147: n=14.
g. Quantifications of number of Bassoon puncta in cryosections of human ALI-COs at different timepoints. Day 56: n=24 regions of interest, Day 69: n=13, Day 84: n=11, Day 97: n=19, Day 125: n=22, Day 147: n=14.
h. Quantifications of number of PSD95 puncta in cryosections of human ALI-COs at different timepoints. Day 56: n=24 regions of interest, Day 69: n=13, Day 84: n=11, Day 97: n=19, Day 125: n=22, Day 147: n=14.
i. Quantifications of number of co-localising bassoon and PSD95 puncta in cryosections of mouse ALI-COs at different timepoints. Day 9: n=10 regions of interest, Day 13: n=27, Day 19: n=21, Day 22: n=27, Day 29: n=21, Day 51: n=17.
j. Quantifications of number of bassoon puncta in cryosections of mouse ALI-COs at different timepoints. Day 9: n=10 regions of interest, Day 13: n=27, Day 19: n=21, Day 22: n=27, Day 29: n=21, Day 51: n=17.
k. Quantifications of number of PSD95 puncta in cryosections of mouse ALI-COs at different timepoints. Day 9: n=10 regions of interest, Day 13: n=27, Day 19: n=21, Day 22: n=27, Day 29: n=21, Day 51: n=17.
l. Quantifications of average mean amplitudes of spontaneous calcium transients in proximal, mid or distal regions of axon tracts of human (day 69) organoid slice cultures in micropatterned devices expressing GCaMP7f. Proximal: n=50 axons, mid: n=43, distal n=58.
m. Quantifications of average event durations of spontaneous calcium transients in proximal, mid or distal regions of axon tracts of human (day 69) organoid slice cultures in micropatterned devices expressing GCaMP7f. Proximal: n=50 axons, mid: n=43, distal n=58.
n. Quantifications of average frequencies of spontaneous calcium transients in proximal, mid or distal regions of axon tracts of human (day 69) organoid slice cultures in micropatterned devices expressing GCaMP7f. Proximal: n=50 axons, mid: n=43, distal n=58.
o. Quantifications of average mean amplitudes of spontaneous calcium transients in proximal, mid or distal regions of axon tracts of mouse (day 15) organoid slice cultures in micropatterned devices expressing GCaMP7f. Proximal: n=23 axons, mid: n=15, distal n=13.
p. Quantifications of average event durations of spontaneous calcium transients in proximal, mid or distal regions of axon tracts of mouse (day 15) organoid slice cultures in micropatterned devices expressing GCaMP7f. Proximal: n=23 axons, mid: n=15, distal n=13.
q. Quantifications of average frequencies of spontaneous calcium transients in proximal, mid or distal regions of axon tracts of mouse (day 15) organoid slice cultures in micropatterned devices expressing GCaMP7f. Proximal: n=23 axons, mid: n=15, distal n=13.
prox, proximal. dis, distal. All data are shown as mean ± SEM; ns $P > 0.05$, *$P < 0.05$, **$P < 0.1$, ***$P < 0.001$ as determined by unpaired *t* tests.

Supplementary Figure 5

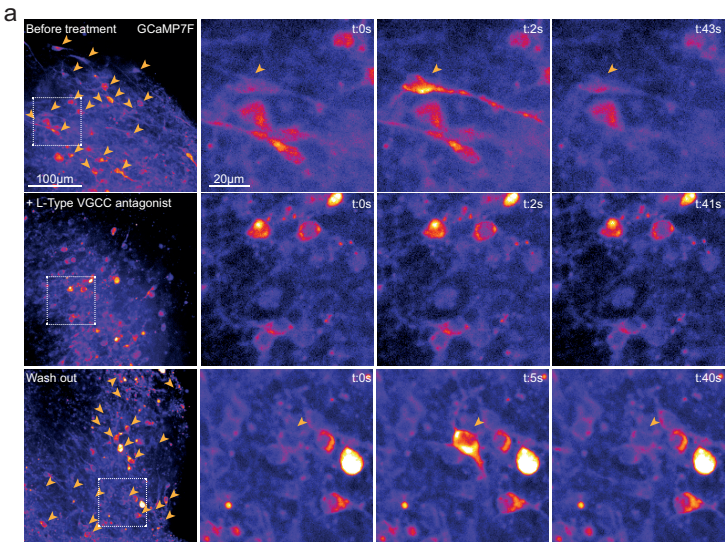

Supplementary Figure 5: L-Type VGCC drive calcium dynamics during axon outgrowth stages and control axon tract length

a. Human (day 96) brain organoid slices in micropatterned devices expressing GCaMP7f before treatment, after 1 hour treatment with nimodipine (L-Type VGCC antagonist) and 3 hours after wash-out of treatment. Arrowheads mark axons showing calcium activity in a five minute timelapse, indicating nearly complete perturbation of calcium dynamics upon L-Type VGCC blocking and full recovery after wash-out. Zooms show stills of representative timelapse of individual neurons (marked by arrowheads).

Supplementary Video 1.

Timelapse of spontaneous calcium transients in an axon tract of a human (day 69) brain organoid slice in micropatterned devices expressing GCaMP7f.

Supplementary Video 2.

Timelapse of spontaneous calcium transients in an axon tract of a mouse (day 15) brain organoid slice in micropatterned devices expressing GCaMP7f.

Supplementary Video 3.

Timelapse of synchronous calcium bursts in an axon tract of a human (day 82) brain organoid slice in micropatterned devices expressing GCaMP7f.

Supplementary Video 4.

Timelapse of synchronous calcium bursts in an axon tract of a mouse (day 19) brain organoid slice in micropatterned devices expressing GCaMP7f.

Supplementary Video 5.

Timelapse of spontaneous calcium transients in an axon tract of a human (day 69) brain organoid slice in micropatterned devices expressing GCaMP7f and treated with DMSO.

Supplementary Video 5.

Timelapse of spontaneous calcium transients in an axon tract of a human (day 69) brain organoid slice in micropatterned devices expressing GCaMP7f and treated with DMSO.

Supplementary Video 6.

Timelapse of spontaneous calcium transients in an axon tract of a human (day 69) brain organoid slice in micropatterned devices expressing GCaMP7f and treated with nimodipine (L-Type VGCC antagonist).

Supplementary Video 7.

Timelapse of spontaneous calcium transients in an axon tract of a human (day 69) brain organoid slice in micropatterned devices expressing GCaMP7f and treated with BayK8644 (L-Type VGCC agonist).

Supplementary Video 8.

Timelapse of calcium activity in a human brain organoid slice (day 96) expressing GCaMP7f before treatment.

Supplementary Video 9.

Timelapse of calcium activity in a human brain organoid slice (day 96) expressing GCaMP7f after treatment with nimodipine (L-Type VGCC antagonist).

Supplementary Video 10.

Timelapse of calcium activity in a human brain organoid slice (day 96) expressing GCaMP7f after washout upon treatment with nimodipine (L-Type VGCC antagonist).

REFERENCES

1. Uzquiano, A. & Arlotta, P. Brain organoids: the quest to decipher human-specific features of brain development. *Curr Opin Genet Dev* 75, 101955 (2022).
2. Libé-Philippot, B. & Vanderhaeghen, P. *Cell*ular and Molecular Mechanisms Linking Human Cortical Development and Evolution. *Annu Rev Genet* 55, 1–27 (2021).
3. DeFelipe, J. The Evolution of the Brain, the Human *Nature* of Cortical Circuits, and Intellectual Creativity. *Front Neuroanat* 5, 29 (2011).
4. Zeiss, C. J. Comparative Milestones in Rodent and Human Postnatal Central Nervous System Development. *Toxicol Pathol* 49, 1368–1373 (2021).
5. Sakai, T. *et al.* Developmental trajectory of the corpus callosum from infancy to the juvenile stage: Comparative MRI between chimpanzees and humans. *Plos One* 12, e0179624 (2017).
6. Semple, B. D., Blomgren, K., Gimlin, K., Ferriero, D. M. & Noble-Haeusslein, L. J. Brain development in rodents and humans: Identifying benchmarks of maturation and vulnerability to injury across species. *Prog. Neurobiol.* 106, 1–16 (2013).
7. Jacobs, B. et al. Regional Dendritic and Spine Variation in Human Cerebral Cortex: a Quantitative Golgi Study. *Cereb Cortex* 11, 558–571 (2001).
8. Huttenlocher, P. R. & Dabholkar, A. S. Regional differences in synaptogenesis in human cerebral cortex. *J Comp Neurol* 387, 167–178 (1997).
9. Felipe, J. D., Marco, P., Fairén, A. & Jones, E. G. Inhibitory synaptogenesis in mouse somatosensory cortex. *Cereb. cortex (N. York, NY : 1991)* 7, 619–634 (1997).
10. Donahue, C. J., Glasser, M. F., Preuss, T. M., Rilling, J. K. & Essen, D. C. V. Quantitative assessment of prefrontal cortex in humans relative to nonhuman primates. *Proc. Natl. Acad. Sci.* 115, E5183–E5192 (2018).

11. Mohan, H. et al. Dendritic and Axonal Architecture of Individual Pyramidal *Neuron*s across Layers of Adult Human Neocortex. Cereb Cortex 25, 4839–4853 (2015).
12. Bianchi, S. et al. Dendritic Morphology of Pyramidal Neurons in the Chimpanzee Neocortex: Regional Specializations and Comparison to Humans. Cereb Cortex 23, 2429–2436 (2013).
13. Schoenemann, P. T., Sheehan, M. J. & Glotzer, L. D. Prefrontal white matter volume is disproportionately larger in humans than in other primates. *Nat Neurosci* 8, 242–252 (2005).
14. Benavides-Piccione, R., Ballesteros-Yáñez, I., DeFelipe, J. & Yuste, R. Cortical area and species differences in dendritic spine morphology. *J Neurocytol* 31, 337–346 (2002).
15. Lindhout, F. W., Krienen, F. M., Pollard, K. S. & Lancaster, M. A. A molecular and cellular perspective on human brain evolution and tempo. *Nature* 630, 596–608 (2024).
16. Lancaster, M. A. Unraveling mechanisms of human brain evolution. Cell 187, 5838–5857 (2024).
17. Diaz-Cuadros, M. et al. Metabolic regulation of species-specific developmental rates. Nature 613, 550–557 (2023).
18. Diaz-Cuadros, M. et al. In vitro characterization of the human segmentation clock. Nature 580, 113–118 (2020).
19. Matsuda, M. et al. Species-specific segmentation clock periods are due to differential biochemical reaction speeds. *Science* 369, 1450–1455 (2020).
20. Rayon, T. et al. Species-specific pace of development is associated with differences in protein stability. Science 369, eaba7667 (2020).
21. Linaro, D. et al. Xenotransplanted Human Cortical Neurons Reveal Species-Specific Development and Functional Integration into Mouse Visual Circuits. Neuron 104, 972-986.e6 (2019).
22. Schörnig, M. et al. Comparison of induced neurons reveals slower structural and functional maturation in humans than in apes. *Elife* 10, e59323 (2021).
23. Otani, T., Marchetto, M. C., Gage, F. H., Simons, B. D. & Livesey, F. J. 2D and 3D Stem Cell Models of Primate Cortical Development Identify Species-Specific Differences in Progenitor Behavior Contributing to Brain Size. *Cell Stem Cell* 18, 467–480 (2016).
24. Iwata, R. et al. Mitochondria metabolism sets the species-specific tempo of neuronal development. Science 379, eabn4705 (2023).
25. Ciceri, G. et al. An epigenetic barrier sets the timing of human neuronal maturation. Nature 1–10 (2024) doi:10.1038/s41586-023-06984-8.
26. Paşca, A. M. et al. Functional cortical neurons and astrocytes from human pluripotent stem cells in 3D culture. *Nat. Methods* 12, 671–678 (2015).
27. Sánchez, D. J. L.-D., Lindhout, F. W., Anderson, A. J., Pellegrini, L. & Lancaster, M. A. Mouse brain organoids model in vivo neurodevelopment and function and capture

differences to human. *bioRxiv* 2024.12.21.629881 (2024) doi:10.1101/2024.12.21.629881.
28. Giandomenico, S. L. et al. Cerebral organoids at the air-liquid interface generate diverse nerve tracts with functional output. Nat Neurosci 22, 669–679 (2019).
29. Dotti, C., Sullivan, C. & Banker, G. The establishment of polarity by hippocampal neurons in culture. *J. Neurosci.* 8, 1454–1468 (1988).
30. Lindhout, F. W. et al. Quantitative mapping of transcriptome and proteome dynamics during polarization of human iPSC-derived neurons. Elife 9, e58124 (2020).
31. Sarnat, H. B. Axonal pathfinding during the development of the nervous system. *Ann. Child Neurol. Soc.* 1, 13–23 (2023).
32. McCormick, L. E. & Gupton, S. L. Mechanistic advances in axon pathfinding. *Curr. Opin. Cell Biol.* 63, 11–19 (2020).
33. Fischer, M. & Kukley, M. Hidden in the white matter: Current views on interstitial white matter neurons. *Neurosci. : a Rev. J. bringing Neurobiol., Neurol. psychiatry* 10738584241282968 (2024) doi:10.1177/10738584241282969.
34. Sedmak, G. & Judaš, M. The total number of white matter interstitial neurons in the human brain. *J. Anat.* 235, 626–636 (2019).
35. Fricker, M., Tolkovsky, A. M., Borutaite, V., Coleman, M. & Brown, G. C. Neuronal Cell Death. *Physiol. Rev.* 98, 813–880 (2018).
36. Gordon, N. Apoptosis (programmed cell death) and other reasons for elimination of neurons and axons. *Brain Dev.* 17, 73–77 (1995).
37. Chiaradia, I. et al. Tissue morphology influences the temporal program of human brain organoid development. Cell Stem Cell 30, 1351-1367.e10 (2023).
38. Lancaster, M. A. et al. Cerebral organoids model human brain development and microcephaly. Nature 501, 373–379 (2013).
39. Leibold, N. S. et al. NMDA receptor activation drives early synapse formation in vivo. bioRxiv 2024.05.23.595343 (2024) doi:10.1101/2024.05.23.595343.
40. Rosenberg, S. S. & Spitzer, N. C. Calcium Signaling in Neuronal Development. *Cold Spring Harb. Perspect. Biol.* 3, a004259 (2011).
41. McKinney, A. A., Petrova, R. & Panagiotakos, G. Calcium and activity-dependent signaling in the developing cerebral cortex. *Dev. (Camb., Engl.)* 149, dev198853 (2022).
42. Gasperini, R. J. et al. How does calcium interact with the cytoskeleton to regulate growth cone motility during axon pathfinding? *Mol. Cell. Neurosci.* 84, 29–35 (2017).
43. Andreae, L. C. & Burrone, J. The role of neuronal activity and transmitter release on synapse formation. *Curr. Opin. Neurobiol.* 27, 47–52 (2014).
44. Hutchins, B. I. & Kalil, K. Differential Outgrowth of Axons and their Branches Is Regulated by Localized Calcium Transients. J. Neurosci. 28, 143–153 (2008).
45. Wen, Z., Guirland, C., Ming, G. & Zheng, J. Q. A CaMKII/Calcineurin Switch Controls the

Direction of Ca2+-Dependent Growth Cone Guidance. Neuron 43, 835–846 (2004).
46. Tang, F., Dent, E. W. & Kalil, K. Spontaneous Calcium Transients in Developing Cortical Neurons Regulate Axon Outgrowth. J. Neurosci. 23, 927–936 (2003).
47. Korkotian, E. & Segal, M. Release of calcium from stores alters the morphology of dendritic spines in cultured hippocampal neurons. Proc. Natl. Acad. Sci. 96, 12068–12072 (1999).
48. Gomez, T. M. & Spitzer, N. C. In vivo regulation of axon extension and pathfinding by growth-cone calcium transients. Nature 397, 350–355 (1999).
49. Moore, S. J. & Murphy, G. G. The role of L-type calcium channels in neuronal excitability and aging. *Neurobiol. Learn. Mem.* 173, 107230 (2020).
50. Correa, B. H. M., Moreira, C. R., Hildebrand, M. E. & Vieira, L. B. The Role of Voltage-Gated Calcium Channels in Basal Ganglia Neurodegenerative Disorders. *Curr. Neuropharmacol.* 21, 183–201 (2023).
51. Lepski, G., Jannes, C. E., Nikkhah, G. & Bischofberger, J. cAMP promotes the differentiation of neural progenitor cells in vitro via modulation of voltage-gated calcium channels. *Front. Cell. Neurosci.* 7, 155 (2013).
52. Lee, D. Global and local missions of cAMP signaling in neural plasticity, learning, and memory. *Front. Pharmacol.* 6, 161 (2015).
53. Hall, D. D. et al. Critical Role of cAMP-Dependent Protein Kinase Anchoring to the L-Type Calcium Channel Cav1.2 via A-Kinase Anchor Protein 150 in Neurons †. *Biochemistry* 46, 1635–1646 (2007).
54. Hergenreder, E. et al. Combined small-molecule treatment accelerates maturation of human pluripotent stem cell-derived neurons. *Nat. Biotechnol.* 1–11 (2024) doi:10.1038/s41587-023-02031-z.
55. Ciceri, G. et al. An epigenetic barrier sets the timing of human neuronal maturation. *Biorxiv* 2022.06.02.490114 (2022) doi:10.1101/2022.06.02.490114.
56. Alfadil, E. & Bradke, F. Moving through the crowd. Where are we at understanding physiological axon growth? *Semin Cell Dev Biol* (2022) doi:10.1016/j.semcdb.2022.07.001.
57. Kandel, E. R. The molecular biology of memory: cAMP, PKA, CRE, CREB-1, CREB-2, and CPEB. *Mol. Brain* 5, 14 (2012).
58. Barbado, M., Fablet, K., Ronjat, M. & Waard, M. D. Gene regulation by voltage-dependent calcium channels. *Biochim. Biophys. Acta (BBA) - Mol. Cell Res.* 1793, 1096–1104 (2009).
59. Munno, D. W., Prince, D. J. & Syed, N. I. Synapse Number and Synaptic Efficacy Are Regulated by Presynaptic cAMP and Protein Kinase A. J. Neurosci. 23, 4146–4155 (2003).
60. West, A. E. et al. Calcium regulation of neuronal gene expression. Proc. Natl. Acad. Sci. 98, 11024–11031 (2001).

61. Kim, J. et al. Human assembloids reveal the consequences of CACNA1G gene variants in the thalamocortical pathway. Neuron (2024) doi:10.1016/j.neuron.2024.09.020.
62. Yu, C. R. et al. Spontaneous Neural Activity Is Required for the Establishment and Maintenance of the Olfactory Sensory Map. Neuron 42, 553–566 (2004).
63. Klocke, B. et al. Insights into the role of intracellular calcium signaling in the neurobiology of neurodevelopmental disorders. *Front. Neurosci.* 17, 1093099 (2023).
64. Pourtavakoli, A. & Ghafouri-Fard, S. Calcium signaling in neurodevelopment and pathophysiology of autism spectrum disorders. *Mol. Biol. Rep.* 49, 10811–10823 (2022).
65. Delhaye, S. & Bardoni, B. Role of phosphodiesterases in the pathophysiology of neurodevelopmental disorders. *Mol. Psychiatry* 26, 4570–4582 (2021).
66. Lorenzon, N. M. & Beam, K. G. Calcium channelopathies. *Kidney Int.* 57, 794–802 (2000).
67. Ferron, L. & Zamponi, G. W. The road to the brain in Timothy syndrome is paved with enhanced CaV1.2 activation gating. *J. Gen. Physiol.* 154, e202213272 (2022).
68. Paşca, S. P. et al. Using iPSC-derived neurons to uncover cellular phenotypes associated with Timothy syndrome. *Nat. Med.* 17, 1657–1662 (2011).
69. Brimson, C. A. et al. Collective oscillatory signaling in Dictyosteliumdiscoideum acts as a developmental timer initiated by weak coupling of a noisy pulsatile signal. *Dev. cell* (2024) doi:10.1016/j.devcel.2024.11.016.
70. Dana, H. et al. High-performance calcium sensors for imaging activity in neuronal populations and microcompartments. Nat. Methods 16, 649–657 (2019).
71. Yau, K. W. et al. Dendrites In Vitro and In Vivo Contain Microtubules of Opposite Polarity and Axon Formation Correlates with Uniform Plus-End-Out Microtubule Orientation. J. Neurosci. 36, 1071–1085 (2016).
72. Sutcliffe, M. & Lancaster, M. A. A Simple Method of Generating 3D Brain Organoids Using Standard Laboratory Equipment. *Methods Mol. Biol. (Clifton, NJ)* 1576, 1–12 (2017).
73. Qin, D., Xia, Y. & Whitesides, G. M. Soft lithography for micro- and nanoscale patterning. *Nat. Protoc.* 5, 491–502 (2010).
74. Brittain, S., Paul, K., Zhao, X.-M. & Whitesides, G. Soft lithography and microfabrication. *Phys. World* 11, 31–37 (1998).
75. Fujii, T. PDMS-based microfluidic devices for biomedical applications. *Microelectron. Eng.* 61–62, 907–914 (2002).
76. Duffy, D. C., McDonald, J. C., Schueller, O. J. A. & Whitesides, G. M. Rapid Prototyping of Microfluidic Systems in Poly(dimethylsiloxane). *Anal. Chem.* 70, 4974–4984 (1998).
77. Preibisch, S., Saalfeld, S. & Tomancak, P. Globally optimal stitching of tiled 3D microscopic image acquisitions. *Bioinformatics* 25, 1463–1465 (2009).
78. Korsunsky, I. et al. Fast, sensitive and accurate integration of single-cell data with

Harmony. Nat. Methods 16, 1289–1296 (2019).
79. Wildenberg, G., Li, H. & Kasthuri, N. The Development of Synapses in Mouse and Macaque Primary Sensory Cortices. Biorxiv 2023.02.15.528564 (2023) doi:10.1101/2023.02.15.528564.
80. Prigge, C. L. & Kay, J. N. Dendrite morphogenesis from birth to adulthood. Curr. Opin. Neurobiol. 53, 139–145 (2018).
81. Haubensak, W., Attardo, A., Denk, W. & Huttner, W. B. Neurons arise in the basal neuroepithelium of the early mammalian telencephalon: A major site of neurogenesis. Proc. Natl. Acad. Sci. 101, 3196–3201 (2004).
82. Cao, J.-W., Liu, L.-Y. & Yu, Y.-C. Gap junctions regulate the development of neural circuits in the neocortex. Curr. Opin. Neurobiol. 81, 102735 (2023).
83. Luhmann, H. J. et al. Spontaneous Neuronal Activity in Developing Neocortical Networks: From Single Cells to Large-Scale Interactions. *Front. Neural Circuits* 10, 40 (2016).
84. Blankenship, A. G. & Feller, M. B. Mechanisms underlying spontaneous patterned activity in developing neural circuits. *Nat. Rev. Neurosci.* 11, 18–29 (2010).